LLE Review
Quarterly Report

July 1982–September 1982

LLE Review

Quarterly Report

July 1982–September 1982

UR
LLE

IN BRIEF

This edition of the LLE Review contains articles which summarize progress in various uniformity experiments on OMEGA, progress in aspects of target fabrication directly related to uniformity and transport studies, and a summary of recent user experiments performed on GDL. Some highlights of the work described in this issue are:

- Achievement of 5% RMS uniformity of irradiation in long-pulse OMEGA target experiments.

- Direct measurement of final core ρR of 2.5×10^{-3} g/cm^2 in Ar-DT targets.

- Improvement of OMEGA beam profile uniformity resulting from a systematic study of stress-induced birefringence in LHG-8 laser rods.

- Successful deployment of ultra low-mass stalks for support of glass microballoon targets in OMEGA experiments.

- The use of biased magnetron sputtering to improve the uniformity of metal coatings applied to glass microballoons.

- The study of the interaction of high-intensity, 0.351-μm radiation with long-scalelength, completely underdense plasmas by measurement of light produced by stimulated Raman scattering.

CONTENTS

OMEGA technician, Dusty Quick, loads the multiple target carousel on the OMEGA vacuum chamber. As many as 16 targets may be selected and positioned without breaking vacuum.

Section 1
LASER SYSTEMS REPORT

1.A GDL Facility Report

The GDL facility continued operations during the fourth quarter of FY82 in support of interaction, x-ray, and damage test campaigns. Continuing support of the interaction experiment was interrupted in August because it became necessary to send the tripler crystals to Inrad for re-polishing and to substitute Koolase™ for the former index-matching fluid, a halocarbon. The crystals have been re-installed, and on September 15, interaction experiments were resumed.

A total of 596 shots was delivered by the facility during the period of July 1 to September 30, 1982. The shot distribution was as follows:

Interaction	206	Shots
Damage Test Facility	265	
X-Ray	64	
Miscellaneous	61	
TOTAL	596	Shots

1.B OMEGA Facility Report

During the quarter July 1 to September 30, 1982, OMEGA activities were largely concerned with conducting the long-pulse (1 ns) campaign. July was spent in the activation and testing of the three-meter oscillator with a newly designed mode-locker. This oscillator demonstrated a very high degree of stability almost as soon as it was activated, and it is the con-

tinued stable performance of the oscillator/driver which has been the most important factor in the smooth, trouble-free administration of this experimental campaign.

The target shots were begun in early August, following a series of calorimeter calibration shots, near-field photography shots, and equivalent target plane photography shots. The two experimental series run during the long-pulse campaign have emphasized (1) the study of irradiation uniformity, with the goal of providing data leading to a beam balance of ~1%, and substantial improvement in beam profile, and (2) transport with the goal of determining burn-through depth, and subsequent mapping of the heat front. Those campaigns have been quite successful, and they still continue.

The following is a summary of OMEGA system shots.

Target Shots	94
Driver Align and Test	112
Beamline c/o and Calibration	91
Miscellaneous	54
TOTAL	351

A very stable, reliable oscillator (see Fig. 1) contributed to the outstanding laser performance during this quarter. It is noteworthy that we

Fig. 1
Oscillator stability histogram.

Pulse-Width Histogram
Long-Pulse Campaign
7/1/82 to 9/30 82
Near-Field Streak Camera

PULSE WIDTH (ps)

E2328
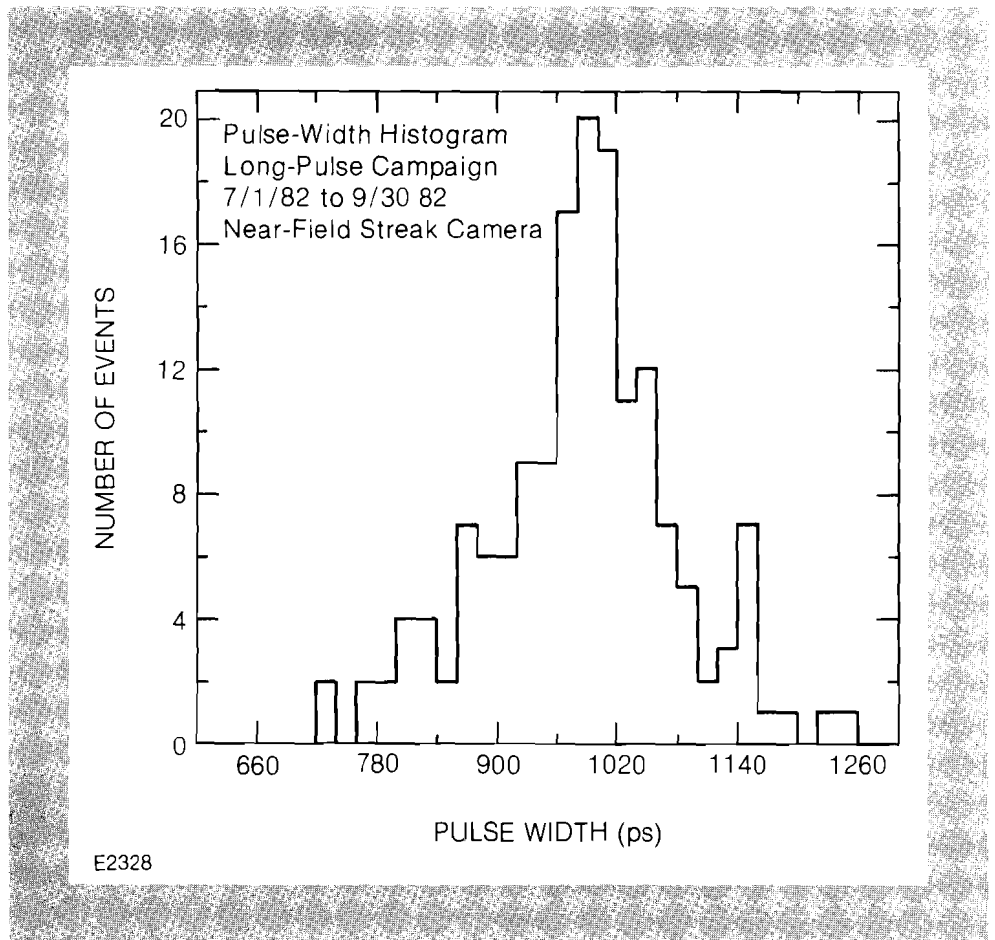
have not lost a single scheduled day's shooting after being relieved of the oscillator/driver problems which plagued us in the past. During the campaign, beam balance has remained in the 7 to 8% vicinity, often dropping below 5% but not exceeding 12%. Total energy has usually been within 10% of that requested and, when it has dropped, energy levels have been restored on the same shooting day.

Beam profiles have generally been acceptable. However, some damage has been sustained by optics in the "A" splitter area, and quotes for replacement of these components are being evaluated. We are also currently investigating some "hot spots" observed near the center of the beam, arising from the driver.

A highlight of the campaign was a tune-up of the driver line including the changing of the oscillator dye concentration, the scrubbing of the laser rods, and the replacing of the glycol coolant to produce an output of 24 joules. This led to target shot number 8081 on September 28 with a total laser energy of approximately 3.2 kilojoules and a beam balance of 6.7%. (This was part of the uniformity series.) Inspection of the system after the shot revealed minor damage sites on the final turning mirrors and focusing lenses due to high-intensity edges on certain beams. However, and more importantly, no damage was observed on Pockels cells or spatial filter lenses, previously considered the weakest links in the system. This system performance does not completely agree with the design code *RAINBOW* (see Fig. 2). Improvements to the numerical model are being investigated. Differences in FWHM measurements of up to 200 ps in near- and far-field streak camera data are also being investigated.

The crystal spectrometers, which are the primary transport diagnostic, have performed during this campaign without the loss of any data. Both soft and NRC streak cameras have been reactivated during this campaign. The Von Hamos spectrometer has taken data during the series, but is currently out of operation for reconfiguration of both film transport and optical systems. The x-ray continuum spectrometer has been completely activated with appropriate k-edge foils, and has acquired its first meaningful data this quarter. A new diagnostic, activated this quarter, was the electron spectrometer. Data acquisition software for the x-ray continuum and the electron spectrometers have been installed, but data reduction software has yet to be implemented. Finally, two charge collectors for the measurement of ion velocities have been implemented.

The development of alignment system software has proceeded with the successful activation of a new, more realistic display of the OMEGA system. The operations task has been reworked somewhat, with work still continuing to make the calorimetry and shot report tasks easier.
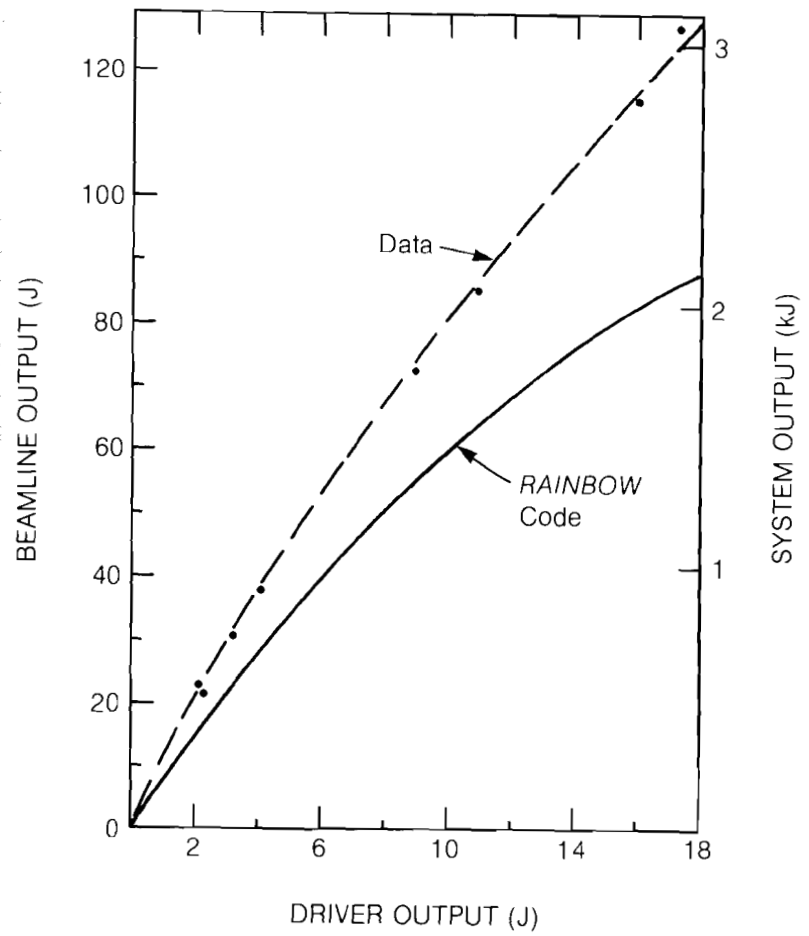
Fig. 2
Beam output versus driver output (actual
and predicted).

Section 2
PROGRESS IN LASER FUSION

2.A Uniformity Requirements for Direct-Drive Laser Fusion

The present objectives of the Drive Uniformity Program at the University of Rochester are (a) to determine the radiation and drive uniformity requirements for directly driven targets, and (b) to achieve the required degree of uniformity with multiple beam irradiation of spherical targets using overlapping beams. This integrated program, which began almost two years ago, has made steady progress in meeting these objectives by the following means:

1) characterizing and optimizing the uniformity of irradiation on the 24-beam OMEGA laser system;
2) conducting experiments to determine the effects of specific, characterized drive uniformity on imploding targets; and
3) comparing the first direct measurements of compressed DT fuel conditions with 1-D and 2-D code calculations to indicate satisfactory low-order symmetry of target implosions.

In considering the necessary irradiation uniformity requirements for direct-drive, the following principal points can be made. For high-compression (1000X) targets a drive uniformity of $\pm 1\%$ is required. The most serious nonuniformities are those with large scalelengths. Large-scalelength nonuniformities in laser irradiation can be smoothed only at high intensities and with long laser wavelengths. Our studies show that it should be possible to attain the required degree of irradiation uniformity by using multiple beams ($n \geq 20$), while maintaining a beam balance (of the order of 5%) and a reasonable individual beam spatial uniformity ($\pm 20\%$).

In this section we will describe the characterization of uniformity on the OMEGA laser system, discuss some of the factors which influence overall irradiation uniformity, and mention some of the measures to be taken to improve it further. The analysis of uniformity is facilitated by decomposing the total irradiation distribution on the target into a set of spherical harmonics or modes. The lowest order modes are directly associated with large-scalelength nonuniformities, and these modes have commanded most of our attention to date.

Multibeam symmetric irradiation of targets places severe requirements on the output characteristics on the laser, especially with regard to beam aiming precision, beam-to-beam energy stability, and uniformity of beam profile. In order to achieve beam placement accuracy, OMEGA routinely places beams on target to within 10 μm of the nominal aim point. This is illustrated in Fig. 3, which shows a reduced x-ray image of a target irradiated specifically to measure aiming accuracy. Symmetric sets of 6-beams are focused onto the surface of a gold-coated sphere, and the spatial coordinates of the resulting x-ray images compared to their expected positions. On all occasions when this test has been made, the RMS pointing error has been no more than 11 μm, well within the margins which insure that beam placement is not a factor in reducing overall irradiation uniformity.

Fig. 3
Isointensity contour plot of the x-ray image from a gold-coated spherical target irradiated by six OMEGA beams focused at the target surface.

- Six-beam surface-focused pointing shots on gold-coated, 200-μm-diameter targets

X-Ray Images of Beam Positions

Predicted Beam Positions
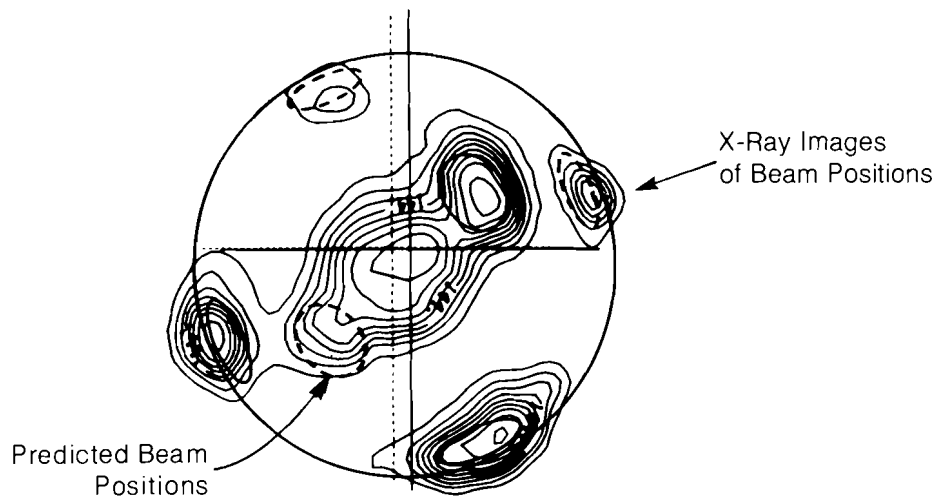
Mean pointing error for 24 beams is 11 μm $\pm$ 6 μm.

E1332

The balance in energy between individual beams is an important factor in determining overall uniformity, particularly the amplitude of the low-order modes that are most difficult to suppress once established in

an implosion. A typical OMEGA beam calorimeter report shows typical individual beam output energies which deviate from the mean beam energy with a peak-to-peak variation of 20%, and an RMS fluctuation of approximately 5%. It is our intention to take measures in the future which will eventually lead to the reduction of this number to the 1 to 2% level. This should satisfy the requirements for uniformity in the low-order modes.

The characterization of the dependence of the uniformity on multiple overlap of individual beam profiles has been extensively studied at LLE. The procedure used to gain an approximate quantification of the energy deposition uniformity is outlined in Fig. 4. The distribution of energy and intensity in the target plane is recorded for each beam on a series of shots, generating a large quantity of data. The two-dimensional beam profiles are individually digitized and an azimuthal average of the intensity distribution obtained. From this data a representative beam profile is obtained, and then used in a pseudo-three-dimensional, spherical, beam superposition code, together with the individual beam energies. This code then computes the uniformity of spherical energy deposition utilizing specific absorption prescriptions for resonance and inverse bremsstrahlung absorption, and incorporates a ray-tracing prescription to account for beams at high angles of incidence to the target surface. The resulting energy deposition uniformity can then be portrayed either as great circle cuts of the spherical distribution, or more usefully by decomposition into simple spherical harmonic modes.

Fig. 4
Procedure used to characterize spherical illumination uniformity.

E1790

7
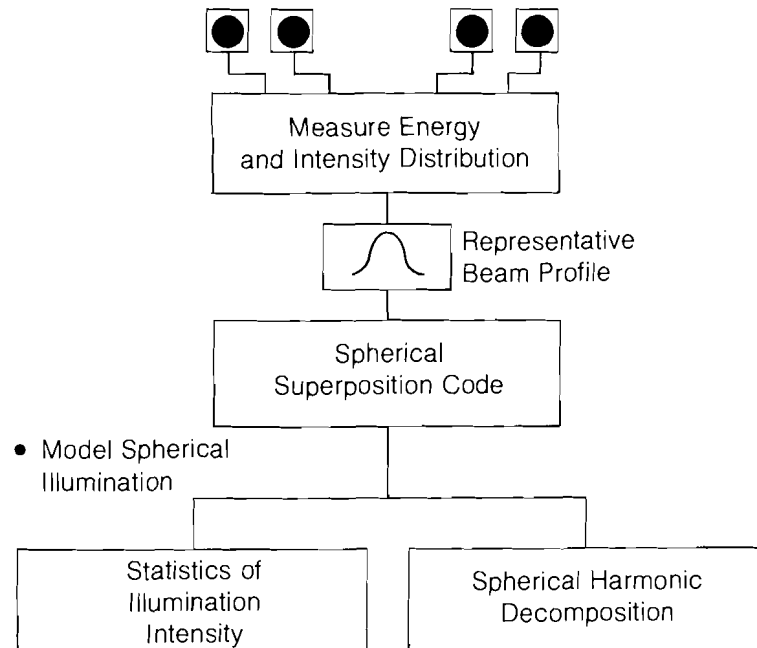
Such an assessment for a typical 24-beam, one-nanosecond target shot with beams focused 10 target radii beyond target center is shown in Fig. 5. The conical beam profile is provided as input into the beam superposition code, which gives a spherical isoenergy deposition distribution plot as shown on the right, and a distribution of amplitudes of the lower harmonic modes shown in the lower plot. It can be seen that apart from the $\ell = 8$ mode, the rms amplitude is typically less than 2%. Since the
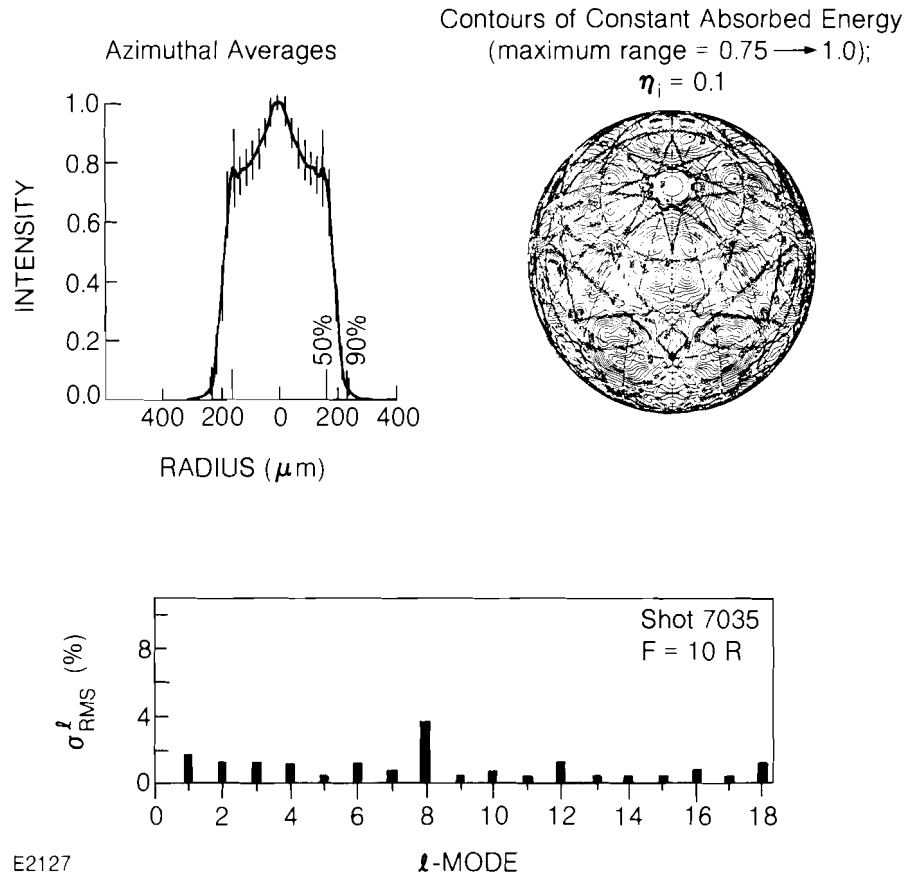
Azimuthal Averages

Contours of Constant Absorbed Energy
(maximum range = 0.75 ⟶ 1.0);
$\eta_i = 0.1$

RADIUS (μm)

E2127

ℓ-MODE

Fig. 5
Model of irradiation uniformity in the OMEGA system.
  a) Azimuthally averaged intensity distribution obtained from equivalent plane photography
  b) Contours of constant absorbed energy obtained from a three-dimensional, numerical ray trace, assuming 24 identical beam profiles of the form shown in (a)
  c) Decomposition of the irradiance distribution into spherical harmonic modes

peak variation of the irradiation amplitude of these modes would be a factor of 3 or more, we have set a goal of improving uniformity by a factor of approximately 5 for future high-compression target experiments.

We must next ask what factors control the intensity profiles of the individual beams and to what extent we can manipulate them to optimize uniformity. We have, through the use of the beam propagation code *MALAPROP*, been able to model the propagation of real beam profiles through the system with high accuracy. The uniformity and radial symmetry of the resulting output beam profile in the equivalent target plane is found to be dependent on (1) the radial and azimuthal gain profiles in all amplifier units, (2) the shape, symmetry, and stability of the input beam profile from the oscillator to the beam line, and (3) the precision of alignment of the individual beams through amplifiers, apertures, and

spatial filters. Preservation of a uniform phase distribution through the entire amplifier chain, the transport optics, and focusing elements to the target is of particular interest to us since the output phase distribution strongly influences the relationship between the output beam distribution in the near field and that in the target plane.

Typical measurements of the radial phase aberration of the output beam—measured by shear-plate interferometry—for various pulse lengths are shown in Fig. 6. It can be seen that for nanosecond pulses, the temporal range in which we are most interested, the oval radial
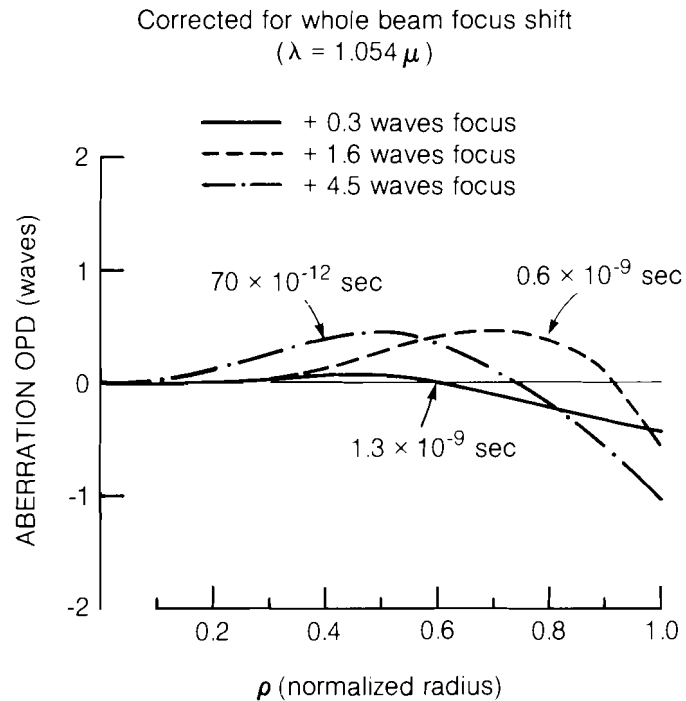
Corrected for whole beam focus shift
($\lambda = 1.054\,\mu$)

——— + 0.3 waves focus
– – – – + 1.6 waves focus
—·—·— + 4.5 waves focus

Fig. 6
Residual aberration of laser beam output for various pulse widths, with account for the whole beam focus shift ($\lambda = 1.054\ \mu m$).

G1007

phase aberration is at most a few tenths of a wave. This radial phase distribution has been used together with measured, near-field intensity distributions to determine, with the use of the propagation code *BEAM-PROP*, the expected intensity distribution in the equivalent target plane (Fig. 7). Comparison of the calculated and measured intensity distributions shows close agreement as demonstrated in Fig. 8.

These studies represent a step forward in characterizing the beam-to-beam intensity distribution; nonetheless, further progress in improving the individual beam profile is both necessary and possible. That this is possible is demonstrated by recent data obtained from the single-beam GDL system. Figure 9 shows the current intensity distribution in the equivalent target plane for infrared light. As can be seen, the azimuthally averaged IR intensity distribution varies locally by no more than 10% and by no more than 15% across the whole beam distribution.
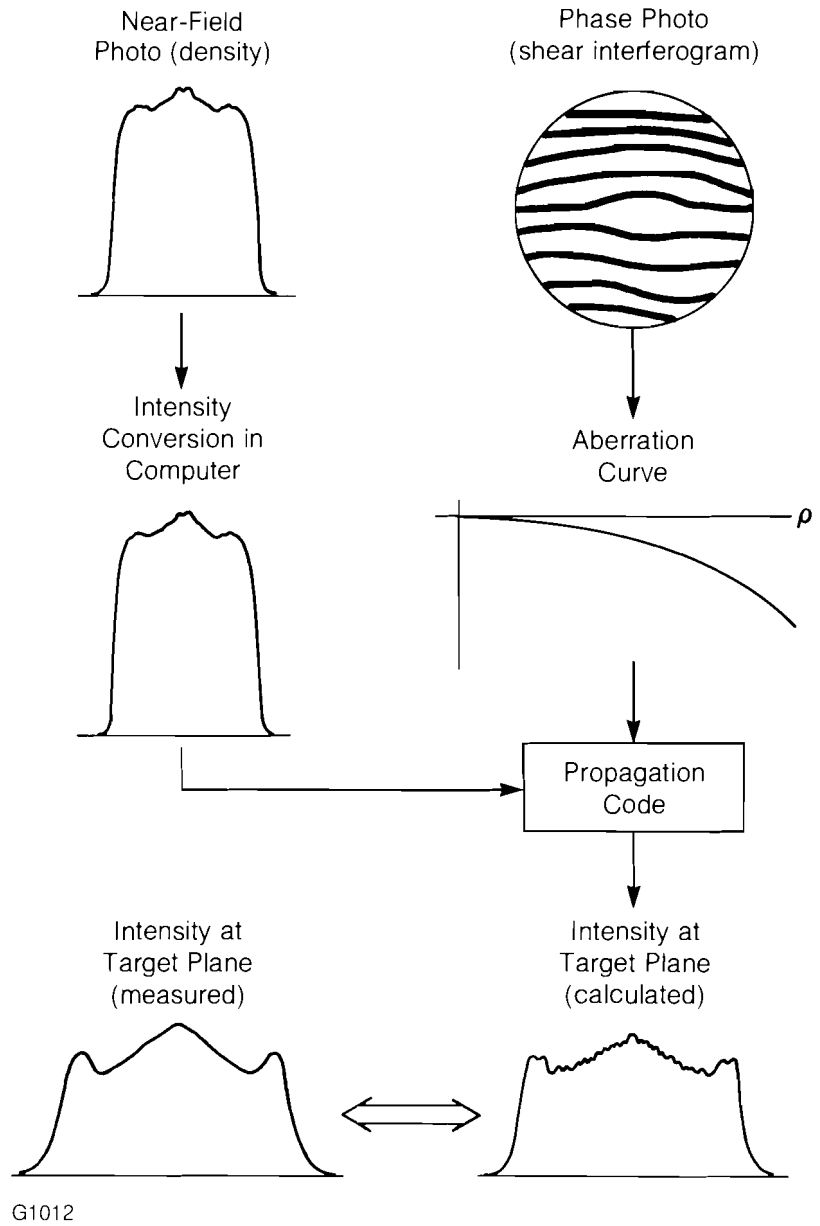
Fig. 7
Procedure used to normalize the beam
propagation code.

Fig. 8
Comparison of single-beam, measured and calculated intensity distributions at the target plane for OMEGA shot number 6369.
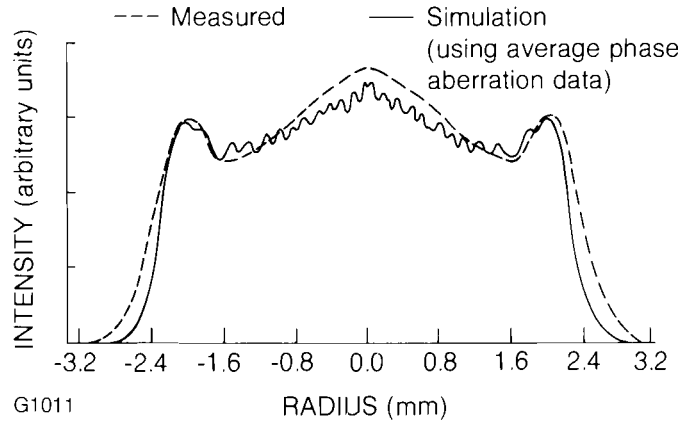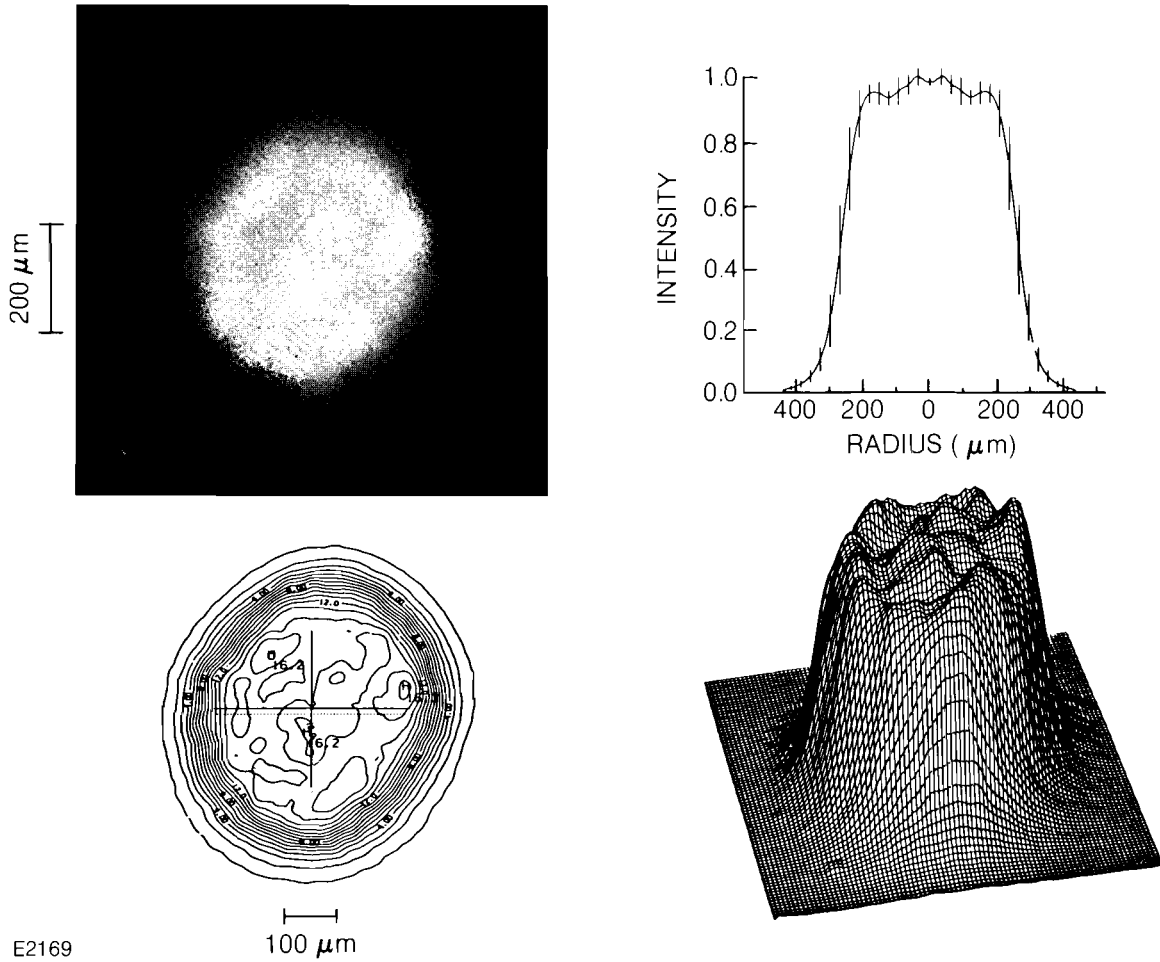

Fig. 9
Target plane intensity distribution obtained from the GDL laser system ($\lambda = 1.054\ \mu m$).

E2169

2.B   24-Beam Implosion of Large-Aspect-Ratio Ar-DT Targets

As part of the program to assess the sensitivity of targets to irradiation uniformity, a number of different classes of DT-filled targets were irradiated under the most uniform conditions that could be achieved, i.e., where the RMS variation in energy deposition was less than 2% in all modes of order higher than eight. Their performance was compared with what one would expect from a perfectly symmetric implosion, deduced from the one-dimensional hydrocode *LILAC*. Target performance in these experiments was assessed through a consideration of the following: (1) analysis of the final core conditions, deduced from x-ray photography of the stagnated shell, (2) a measurement of the final core ρR, and (3) the use of a number of x-ray spectroscopic techniques, some of them novel. In this section, we describe one set of these experiments performed on large-diameter targets having initial aspect ratios as high as 275, at moderate intensities (1 to 4×10^{14} W/cm^2) with nanosecond pulses. In this range of intensity, inverse bremsstrahlung is the dominant mechanism of absorption, and with moderate energy loading of the order of 0.5 J/ngm, the shell achieves a peak velocity of the order of 1.5×10^7 cm/sec, before stagnating with a volumetric compression of the order of 300.

A typical x-ray photograph of one of these targets during irradiation is shown in Fig. 10. This particular target was overcoated with 5 μm of CH.

Fig. 10
X-ray micrograph of imploded argon-DT-filled target recorded in the 1 to 2 keV range (shot 7235). The target was a 400-μm-diameter glass microballoon with a 1.1-μm wall thickness and a 5-μm-thick plastic (CH) coating. It was filled with 20 atmospheres of DT and 2 atmospheres of argon. The total incident laser energy was 2.06 kJ (24 beams) with a pulse width of approximately 1 ns. The beams were focused 8 target radii behind target center.

X-RAY IMAGE OF 1-2 keV EMISSION

Shot 7235
Incident Energy ~2.06 kJ
Pulsewidth ~0.996 ns
24 Beams
Focus 8 R

Diameter = 400 μm
Glass Microballoon
20 atm DT
2 atm Ar
Wall = 1.1 μm
CH Over Layer = 5 μm
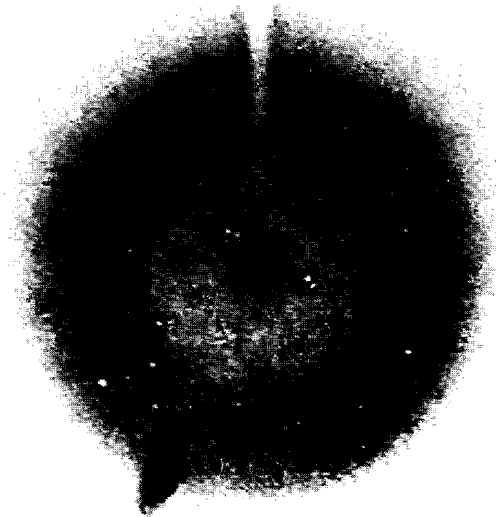
E1856

The extent of the ablation region during the laser pulse is shown by the radial extent of the annular emitting region. X-ray emission from the central core is clearly identified as being from Ar, Si, and Ca line emission, as will be shown later. The cooling effect of the 20-μm stalk can be clearly seen and the high-Z glass plug used to reseal the glass microballoon after Ar filling, can be identified.

The final ρR of the DT fuel was measured by a technique illustrated in Fig. 11. This technique analyzes the spectrum of deuterons and tritons elastically scattered off MeV neutrons in the core. The number of such scattered-reaction-product particles is directly proportional to the neutron yield, and to the density and the extent of the compressed core. CR-39 nuclear track detector material was used to detect the scattered deuterons and tritons. This material is a sensitive detector of high-velocity particles; the track diameter, under controlled etch conditions, is dependent on the original energy of the particle. The detector was maintained at atmospheric pressure in a special capsule deployed in the target chamber. A tantalum foil was used to discriminate against the effects of x-ray radiation and low-energy ions.

E1855
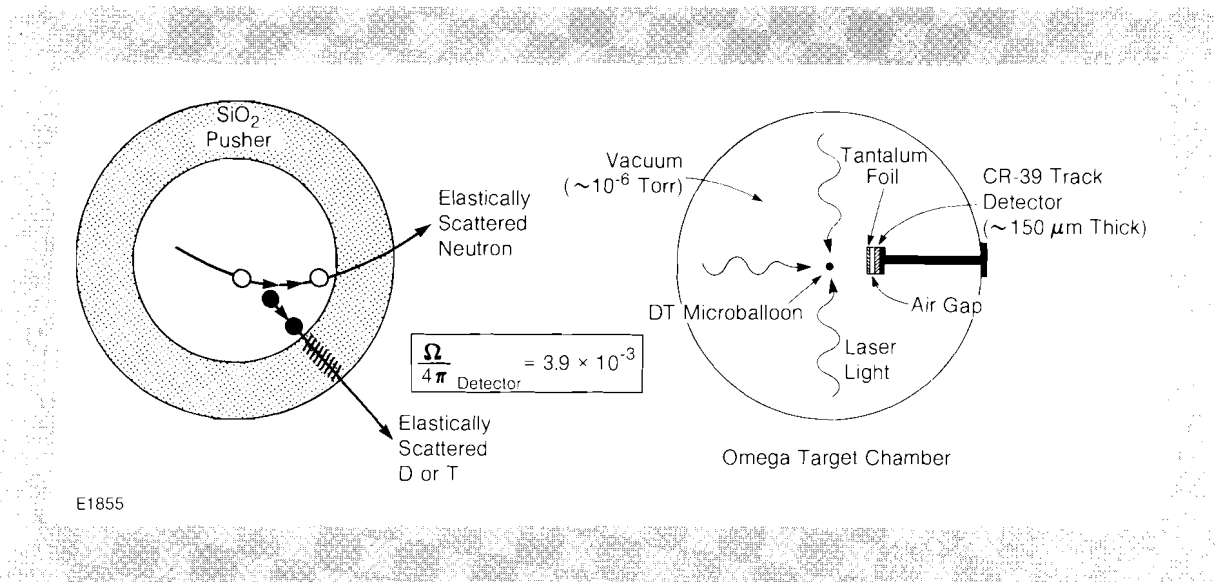
Fig. 11
Schematic illustration of the use of elastically scattered neutrons, deutrons, and tritons in the determination of compressed core conditions.

The thickness of the foil filter determines the range of deuterons and tritons which may be detected, and the use of several detectors with different filters permits us to determine the total, combined spectrum of deuteron and triton, as shown in Fig. 12. Discrimination against the 14-MeV protons is effectively made by utilizing 100-μm-thick plates of CR-39, in which the proton has little range. However, the scattered hydrogenic ions have sufficient energy to pass right through the detector providing coincident etched tracks on each side of the detector. Thus, the total recorded track spectrum for a typical Ar-DT shot is as shown in Fig. 13. Here the lower etched region shows the spectrum of coincident tracks resulting from deuterons and tritons, whereas the upper etched region shows the added counts from noncoincident tracks resulting primarily from 14-MeV protons. The resultant value of ρR deduced from this spectrum and from the known yield was 2.6×10^{-3} g/cm^2 with a statistical error of 15%.

Triton Window

Deuteron Window

Triton Peak

Deuteron Peak

50 μm T_a

95 μm T_a

75 μm T_a

115 μm T_a

KNOCK-ON SPECTRUM

E/A (MeV)

E/A (MeV)

E1461a
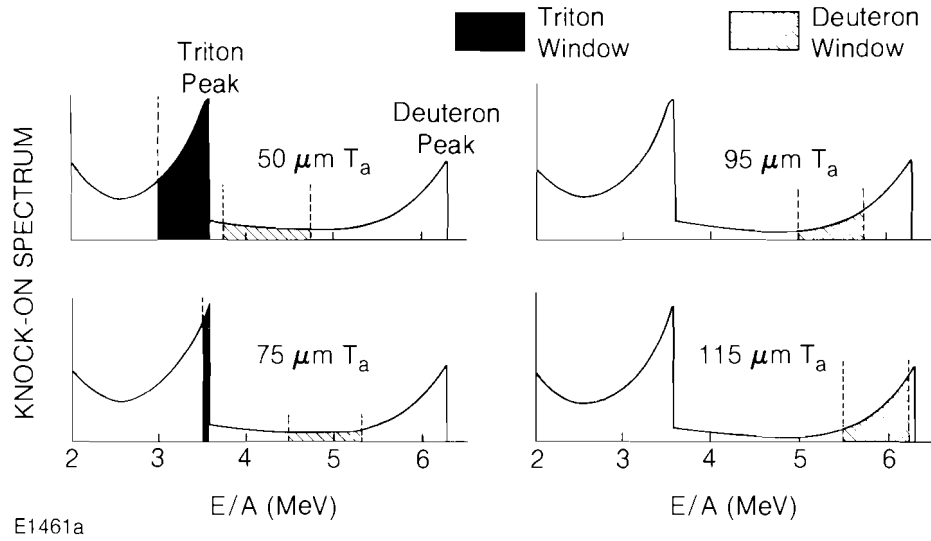
Fig. 12
Illustration of the effective response windows of various foil-filtered, CR-39 track detectors for elastically scattered core reaction products.

Shot 7219
Energy on Target = 2.15 kJ
Pulsewidth = 1044 ps
24 Beams
Focus = 8 R

Diameter = 414 μm
Wall = 0.84 μm
20 atm DT
2 atm Ar

$Y_n = 1.4 \times 10^8$

$\rho R = (2.6 \pm 0.4) \times 10^{-3}$ gm/cm^2

TOTAL NUMBER

TRACK DIAMETER (μm)

Total Number of Coincidence Tracks = 63

E1858
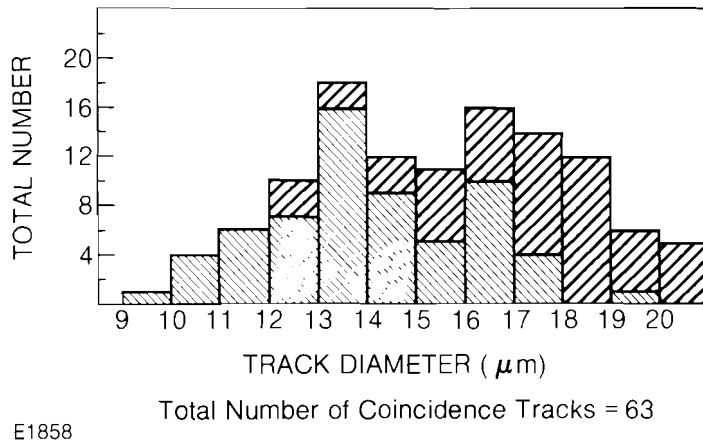
Fig. 13
Reaction-product track spectrum from shot 7219. The target was a 414-μm-diameter glass microballoon with 0.84-μm wall thickness. It was filled with 20 atmospheres of DT and 2 atmospheres of argon. The total incident laser energy was 2.15 kJ (24 beams) with a pulse width of 1.044 ns. The beams were focused 8 target radii behind the target center. The neutron yield was 1.4x10^8.

Spectroscopic techniques provide an alternative approach to the direct measurement of ρR. Figure 14 shows a typical Ar spectrum from this type of target. Although the Ar-L_α line is optically thick in this range of ρ and ρR, the Stark broadening ~16eV of the L_β line (although not totally optically thin) would indicate a maximum Ar density

400 μm Diameter Glass Shell
Wall Thickness ~1 μm
24 Beam Irradiation at F = 8 R
2 kJ Incident in 1 ns

PHOTON ENERGY (keV)

E1860

Fig. 14
Argon x-ray line emission spectrum from the target used in shot 7219 (Fig. 13). Detailed analysis of the lineshape of the argon Lyman-β emission permits a density of 0.7 g/cm³ to be deduced.

of 0.7 g/cm³. An estimate of the opacity effect has recently been formulated which predicts that it has at best a 10% effect on the calculated value of the density. This formalism also provides an estimate of the Ar $\rho R \sim 2.5 \times 10^{-3}$ g/cm².
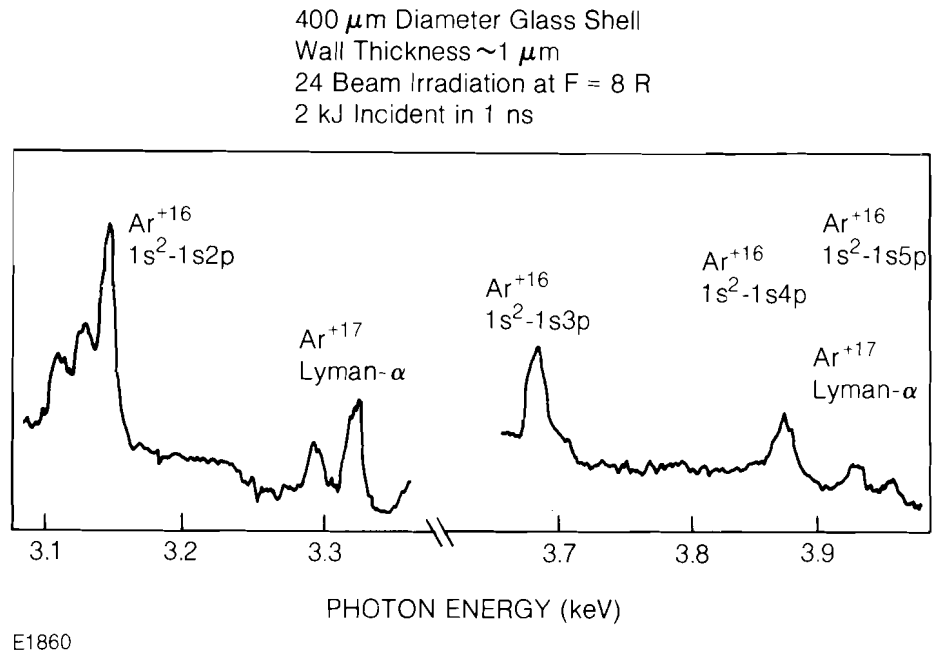
These values are supported by monochromatic x-ray microscopy of the extent of the Ar emission region obtained with the instrument shown in Fig. 15. A fine (2d = 3000 Å) free-standing gold transmission grating, together with a 100-μm slit, is imposed within the optical path of a Kirkpatrick–Baez microscope providing two-dimensional microscopic images of the emitting regions of specific lines. Thus, each mirror combination of the Kirkpatrick–Baez microscope produces a conventional zero-order image resulting from undispersed x-rays in the microscope. On each side of the zero-order image are displayed the first- and second-order images of line emission emitted from the target. A typical image of an Ar-D₂ target is shown in Fig. 16. The large circular area of diffuse x-ray emission in the center of the image results from the deliberately overexposed zero-order image. On either side can be seen distinct images of the ≃ 4keV Ar resonance line emission, and also that of the Si x-ray emission originating from the core of the target. The spatial extent of the Ar emission is ~40 μm, whereas the Si emission originates from a somewhat larger region (~80 μm), as one would expect. These photographs of the emitting region of the Ar imply final values of the Ar density radius product ~2.5×10⁻³ g/cm², in close agreement with the value determined for DT from scattered reaction product spectrometry.

Similar values for the extent of the emitting region of x-rays from the diagnostic gas in the core can be deduced from space-resolved x-ray

15
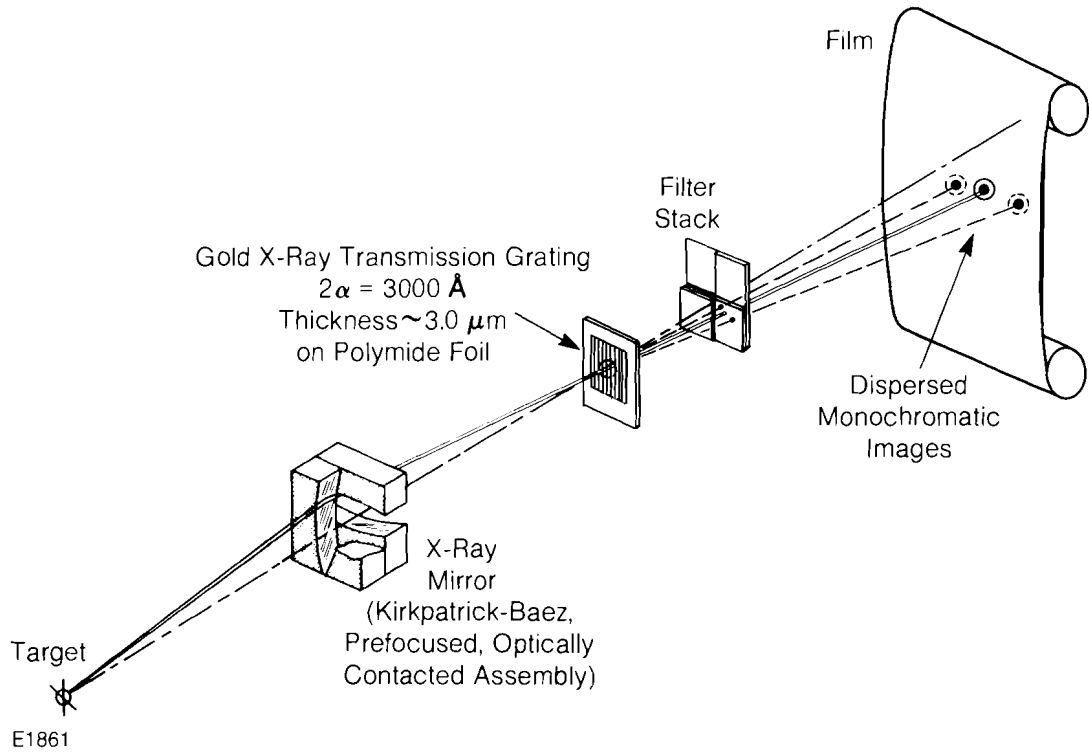
Fig. 15 Schematic of the use of a soft x-ray transmission grating (supplied by NLUF users) with the LLE K-B x-ray microscopy to obtain spatially and spectrally resolved images of imploded targets.

Shot 6995
24-Beam Irradiation
Diameter = 396 μm
Wall = 0.82 μm
Glass Microballoon
2 atm Ar
20 atm D_2

2.04 kJ
996 ps
Target mass = 1217 ngm
Focus = 8 R
Beam Balance = 8.7%
η_a = 38.7%
Y_n = 2.0 × 10^6

E1854

X-R MICROSCOPE IMAGE

Ar   Si

80 μ

400 μ

Fig. 16   X-ray images of an argon-D_2-filled target obtained with the system shown in Fig. 15.

spectroscopy. This is illustrated in Fig. 17 which shows the spatial profiles of Si- and Ne-L_α lines from the compressed core of a 400-μm-diameter D_2 Ne-filled target. As the figure demonstrates, the spatial extent of the Ne is ~50 μm, whereas Abel inversion of the Si emission yields a ring having a diameter of approximately 100 μm.
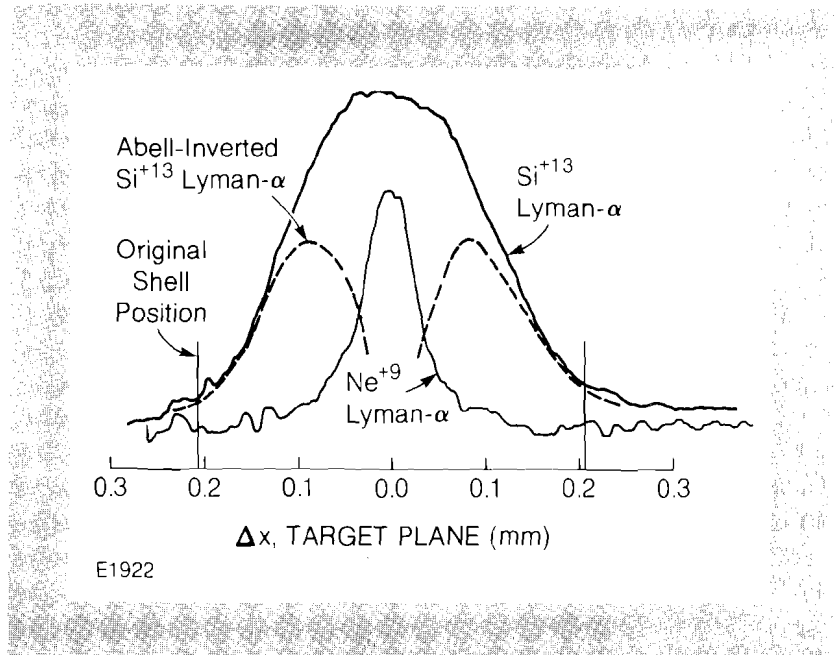
Fig. 17
Spatially resolved x-ray line emission from various target components in a D_2 + 10% neon-filled target.

The experimentally determined parameters of the final core state and the predictions of the one-dimensional hydrocode LILAC are in reasonable agreement. Table 1 shows experimentally and theoretically determined values for the Ar-DT target shot illustrated in previous figures. The

$=====$ SHOT 7219 $=====$
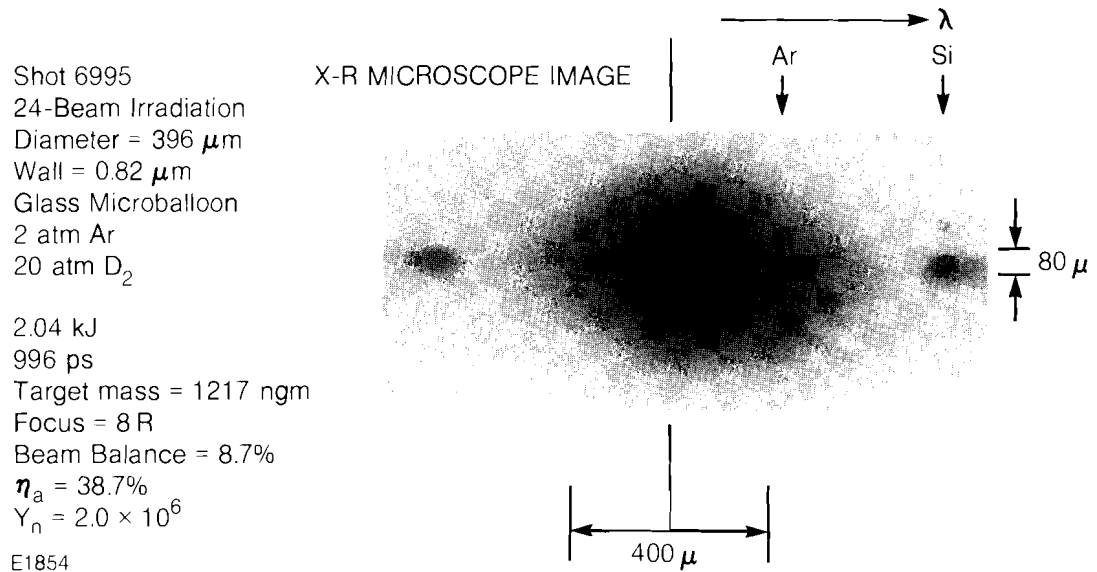
LASER PARAMETERS

Input Power: 2.1 TW
Pulse Length: 1.04 ns

TARGET PARAMETERS

Fuel: DT (20 atm); Ar (2 atm)
       201 μm radius
Pusher: 0.84 μm glass

	Experiment	LILAC Simulation
Absorption	0.37	0.36
Neutron Yield Y_n	2.0×10^8	1.4×10^8
DT density (g/cm^3)	0.7	1.0
Ar density (g/cm^3)	0.7	1.0
R core (μm)	35	30.0
ρR (DT) (mgm/cm^2)	2.6 ± 0.4	3.0
ρR (Ar) (mgm/cm^2)	2.5 ± 0.5	3.0
ρR (Total) (mgm/cm^2)	5.1	6.0

E2157

Table 1
Comparison of OMEGA experimental results with LILAC simulation of large-aspect-ratio target implosion. The comparison is made using the laser and target parameters from shot number 7219.

one-dimensional hydrosimulation was made on the basis of predominantly inverse bremsstrahlung absorption with a flux-limited thermal transport model (f = 0.05), and with a deposition into fast electrons of 10% of that energy reaching the critical density surface. This implied, typically, that no more than 2% of the absorbed energy would be deposited into fast electrons. As we can see, there is substantial agreement between the measured absorption and the neutron yield predictions. The experimentally determined values of the final core density and radius are well bracketed by the predictions of the one-dimensional code. The variability in the final values of the core density and radius predicted from *LILAC* arises as a consequence of the rapid variation of ρR around the time of peak compression. The strong calculated variation in ρR in this simulation is shown in Fig. 18. The difference between the measured total ρR value and that predicted at the time of peak neutron production is a factor of 2. The difference in time between these two points on the ρR curve is $\sim$100 ps. Although the one-dimensional code predicts the experimentally determined values of the core density and radius very well, the rapid changes in these parameters around peak compression emphasizes the need for more detailed time-resolved diagnostics of the final core state.

Shot 7219   2 atm Ar
24-beam irradiation   20 atm DT
Diameter = 414 μm   E = 2.15 kJ
Wall = 0.86 μm t_L = 1.044 ns

E2516
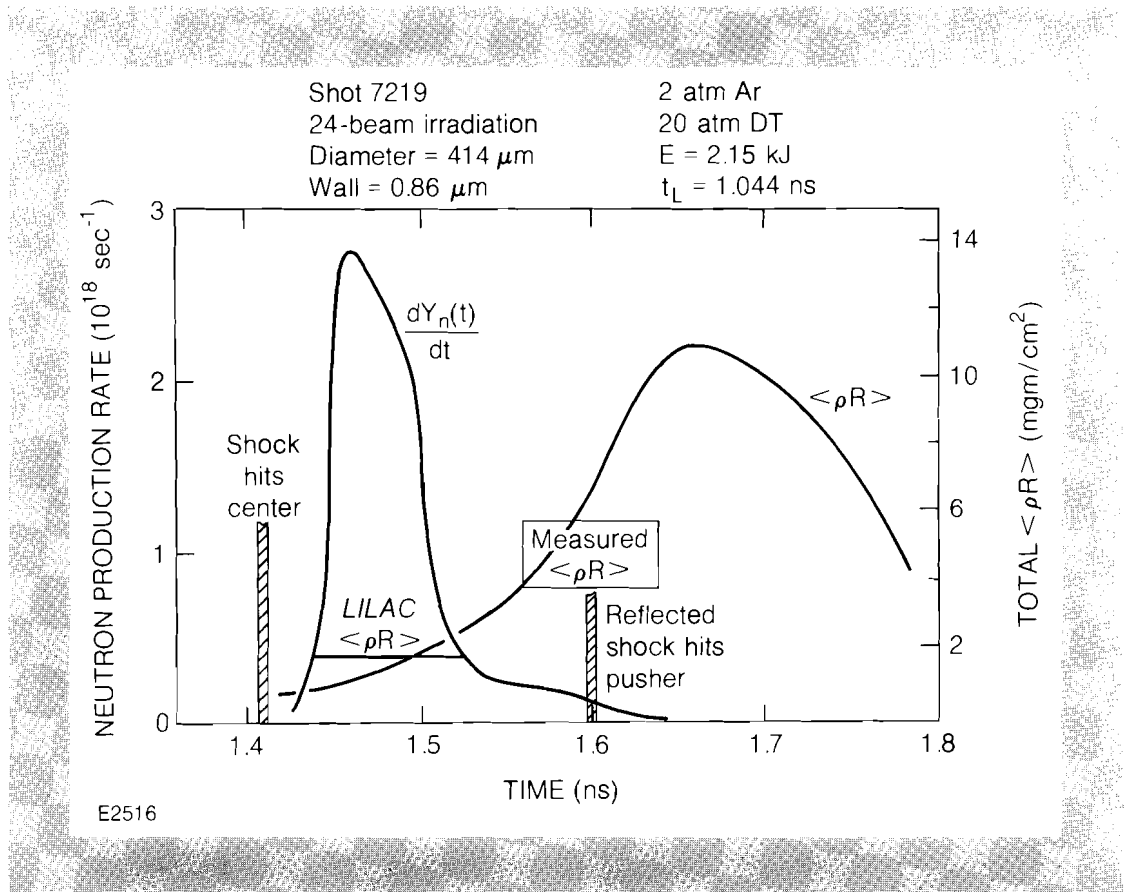
Fig. 18
Calculated time-histories of neutron yield and core $<\rho R>$ for shot 7219 (also discussed in Figs. 13 and 14).

We have described some initial experiments on Ar-seeded, large-diameter, high-aspect-ratio, DT-filled, glass microballoons irradiated with nanosecond pulses from the 24-beam OMEGA facility at moderate intensities. Measurements of the final core conditions through x-ray microscopy, core-reaction-product spectrometry, and time- and space-re-

solved x-ray spectrometry have shown that the final core state is in reasonable agreement with the prediction of the one-dimensional hydrocode. They thus imply a reasonably high level of symmetry in the shell implosion. In addition, we report the independent estimate of the final core ρR product by two separate techniques; this is a diagnostic development which should find many applications in future experiments.

2.C Stress-Induced Birefringence in the Nearly Athermal Glass LHG-8

Recent[1] theoretical estimates of the target illumination uniformity required for direct-drive experiments have assumed azimuthally symmetric beam profiles. In order to match those assumptions as closely as possible in experiments on the OMEGA laser system, a study was initiated to identify sources of azimuthal beam asymmetry. This program has improved our understanding of stress-induced birefringence in rods of the nearly athermal glass LHG-8 used in OMEGA. Nearly athermal glasses are so called because the change in index, n, with temperature is approximately opposite to the change in the product of (n − 1) times the coefficient of expansion. Such glasses do not exhibit the usual large change in optical path with a change in temperature. However, they still show birefringence due to stresses created by radially non-uniform pumping. In what follows, only rod geometries with azimuthal symmetry are considered. End effects are also ignored.

A rod with an azimuthally symmetric temperature profile behaves as a waveplate with principal axes in the radial and tangential directions. Using Quelle's formalism,[2] it is possible to calculate the change in optical path for radial and tangential polarizations in a thermally stressed rod from those of an isothermal rod. The needed parameters are Young's modulus, Poisson's ratio, the coefficient of thermal expansion, the change in index with temperature, the photoelastic constants, and the temperature profile. If all that is wanted is path difference between radial and tangential polarizations, i.e., the birefringence, only the difference between the photoelastic constants is needed. The only parameter that is usually unknown is the temperature profile. Based on confidence established in one-dimensional simulations of the stored energy and heat deposition in active-mirror amplifiers, we approximated the temperature profile in 40-, 64-, and 90-mm-diameter rod amplifiers as a constant times the small-signal gain profiles. This was particularly convenient as the rod radial gain profiles are routinely measured. The one-Cartesian-dimension pumping simulations assume that the deposited heat is due to Nd ion absorption from 340 to 900 nm, and to undoped glass absorption from 340 to 700 nm. There are several Nd contributions that must be counted in the heating calculation. They are:
   1) the so-called quantum defect, which is the energy difference between the absorbing Nd energy level and the $4F_{3/2}$ upper lasing level. The cascade to the upper lasing level is assumed to be phonon-dominated (little fluorescence);
   2) cooperative relaxation among adjacent excited and unexcited Nd ions; and

3) phonon-assisted decay from the 4I levels to the ground state after fluorescence from the $4F_{3/2}$ level.

For the 0.54 wt-% doped sample of LHG-8 pumped by the flashlamps used in the rod amplifiers, the simulations predict that, on the spatial average, at the time of peak gain, for every joule of stored energy in the form of inversion, there should be approximately 1.9 joules of deposited heat, primarily from the quantum defect. This is a lower bound as UV and IR glass absorption has been ignored. If this number is used to calculate the stress-induced birefringence in the aforementioned rods, small amounts of birefringence are found.

To measure the active birefringence, the amplifiers were placed on a translation stage between crossed polarizers. A collimated He-Ne probe with a Gaussian beam intensity distribution having approximately 1-mm FWHM was carefully aligned parallel with the rod edge. The wavelength dispersion of stress birefringence was assumed to be small. A large-area photodiode intercepted the transmitted light. The output of the photodiode was monitored on an oscilloscope and data was taken by a sampling digital voltmeter accurately timed to sample at the fluorescence or gain peak of the rod under test. Prior to each shot, the transmission of the rod was measured with the polarizers parallel. This allowed the normalized transmission at gain maximum to be calculated, and from it, the birefringence. A minimum of two measurements were made at each of approximately eight radial locations in every rod. The rods were cooled by a 50%/50% solution of ethylene glycol and water. A strip chart recorder was connected to the photodiode output to be sure rethermalization was complete before the next measurement. A scan started at the edge of the rod and proceeded inward until the measured birefringence fell below 0.5 nm/cm.

One 40-mm rod, two 64-mm rods, and one 90-mm rod were tested. The smaller rods all had the same Nd-doping of 0.54 wt-% while the 90-mm rod was doped at 0.39 wt-%. The 40-mm rod was pumped at 75% of the bank energy of the others. The two 64-mm rods were identical except that #530B had undergone over 500 system shots before it was removed for birefringence testing.

The measured birefringence in nm/cm versus distance from the rod edge is plotted for three of the rods in Fig. 19. Also shown for the three rods is the least squares best fit that was made by varying the constant of proportionality between the measured stored energy profile and the assumed temperature profile used in Quelle's model. As expected, the 40-mm rod exhibited the largest temperature change per unit radius, and exhibited the greatest birefringence. The 90-mm rod exhibited the least temperature change, and the least birefringence. Each cross represents one data point. Since three shots at the most were taken at a single location, no statistics were generated and no error bars were assigned in the vertical direction. The radial position was always known to within ± 0.5 mm and corresponds approximately to the size of the cross in the horizontal direction.

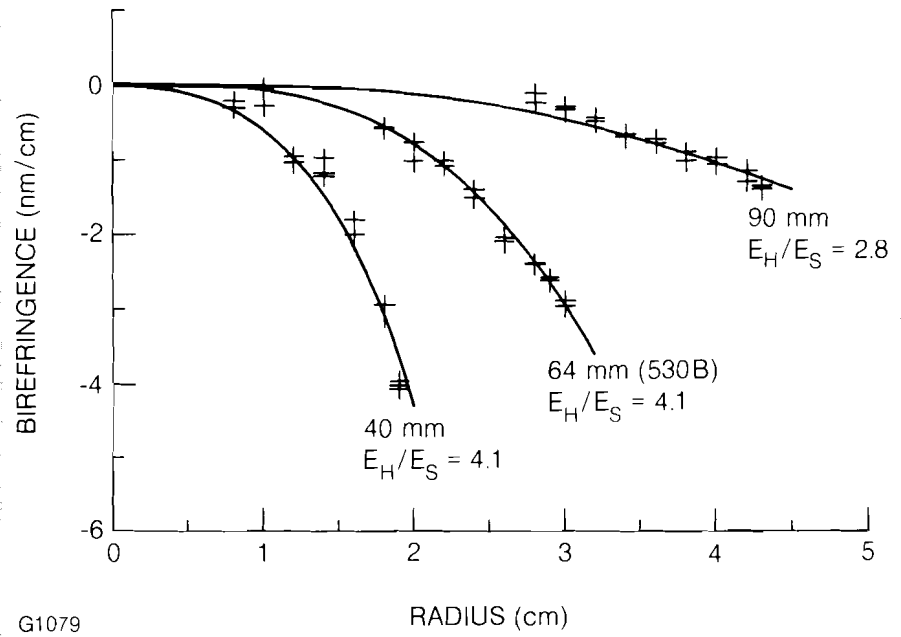Figure 20 compares the active birefringence of the two 64-mm rods

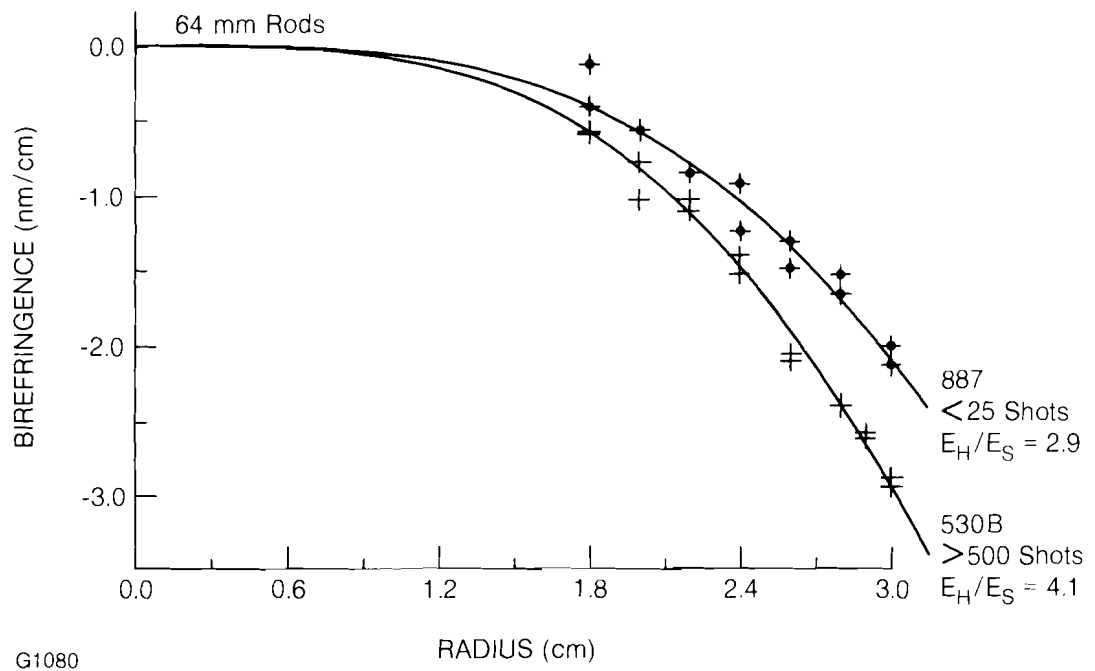Fig. 19 Radial variation of active birefringence in various OMEGA system laser rods.

Fig. 20 Radial variation of birefringence in a used (#530B) and an unused (#887) 64-mm-diameter laser rod.

tested. The unused rod displays less birefringence than the used one. The constants of proportionality are 2.9 and 4.1 respectively. A similar difference exists between the constants of proportionality of the 90-mm and the 40-mm rods. The 90-mm rod, with approximately 350 system shots on it, reaches the best fit with a constant of proportionality of 2.8 whereas the 40-mm rod, with many shots, has a constant of 4.1. It is possible to attribute the difference to increased absorption due to solarization, but the definitive test will be to measure the birefringence of a new rod, and remeasure it after it has been subjected to several hundred system shots.

For the 64-mm rods, the one-dimensional pumping simulations predict a constant of proportionality between the stored energy density and the deposited heat of 1.9. The measurements here show 2.9 for a new rod. This difference is not totally unexpected since the simulations include Nd absorption and undoped glass absorption while they neglect absorption associated with the UV absorption edge of the glass as well as any infrared absorption. The measured active birefringence for all three-diameter rods has been incorporated into laser system modeling codes.

The OMEGA laser is an all-rod system. It consists of a driver line of four rods, one each of 16-, 30-, 40-, and 64-mm diameter. The driver is split horizontally into six beams; then each of these passes another 64-mm rod, the so-called "A" head. Each of the six beams is further split vertically, then horizontally, to yield 24 beams; each of these then passes a 64-mm and 90-mm rod.

In the cases studied here, the active birefringence in LHG-8 rods is small. Even in the 40-mm rod, the measured active birefringence leads to only a 14% reduction in transmission at rod edge through parallel polarizers. Only in the following special circumstances has it become a large effect.

The first example is from the driver-line, 40-mm stage. Originally, the beam throttle consisted of a half-wave plate located upstream of the 40-mm amplifier head which rotated the polarization of the beam through an angle 2θ (where θ is the angle between the fast axis of the plate and the transmission axis of the polarizer) so as to reject some of it on the Pockels cell polarizer following the rod. Near-field photographs which showed a square beam outline are explained by the active birefringence in the 40-mm rod. Figure 21 shows the output of the driver at full throttle ($\theta=0°$), and at 12% output ($\theta=35°$). At full output, there is some modulation at the beam circumference which is partially due to modulation of the input beam. At $\theta=35°$, at locations in the rod where the input polarization happens to be oriented at 45° to the r- (radial) and theta-directions, 12% of the input beam is transmitted while 88% of the light which is orthogonally polarized due to retardation is transmitted. These two components combine linearly in the ratio of 2:1. At locations where the input polarization is parallel to either the r- or theta-directions, no retardation occurs and the 12% of the input is transmitted. This latter condition occurs at $\theta=70°$ and $\theta=-20°$ from the vertical reference and leads to minima in the transmitted intensity which we observe in the

Half Waveplate Angle θ from Vertical

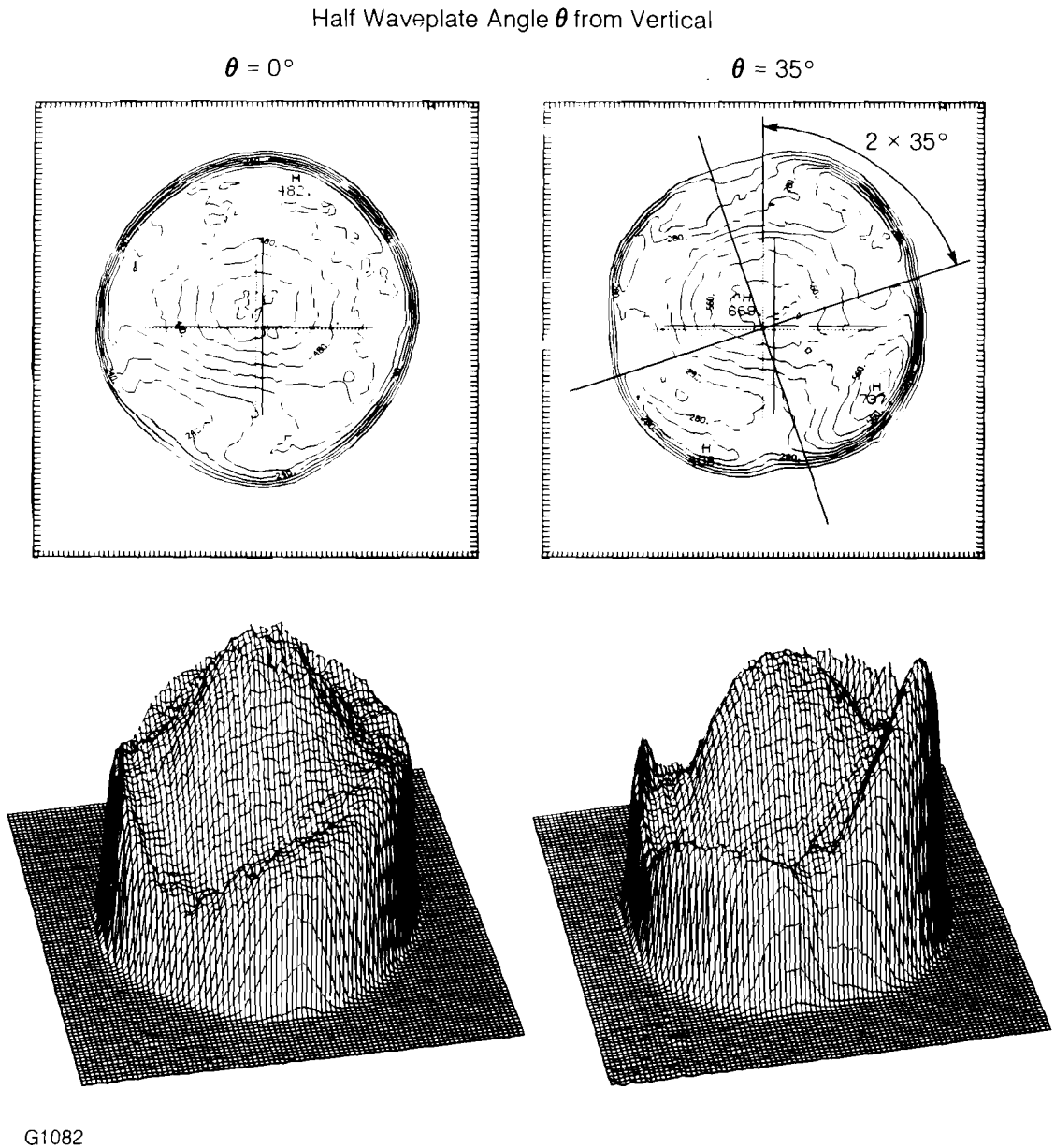| $\theta = 0°$ | $\theta = 35°$ |

G1082

Fig. 21
Intensity distribution from the original
OMEGA driver line at full throttle.

near field. Finally, if one sets the fast axis of the half-wave plate to 45°, one expects to see only the orthogonal component of the 40-mm stage again located where the input polarization to the rod is at 45° to the r- and theta-axes. This is clearly seen in Fig. 22. (Note here that the film exposure was saturating on the peak-intensity part of the beam.) The variation in the height of the four peaks is probably due to the miscentering of the beam in the rod.

The OMEGA system has since been reconfigured to eliminate this problem by locating the throttle plate further upstream in the system.
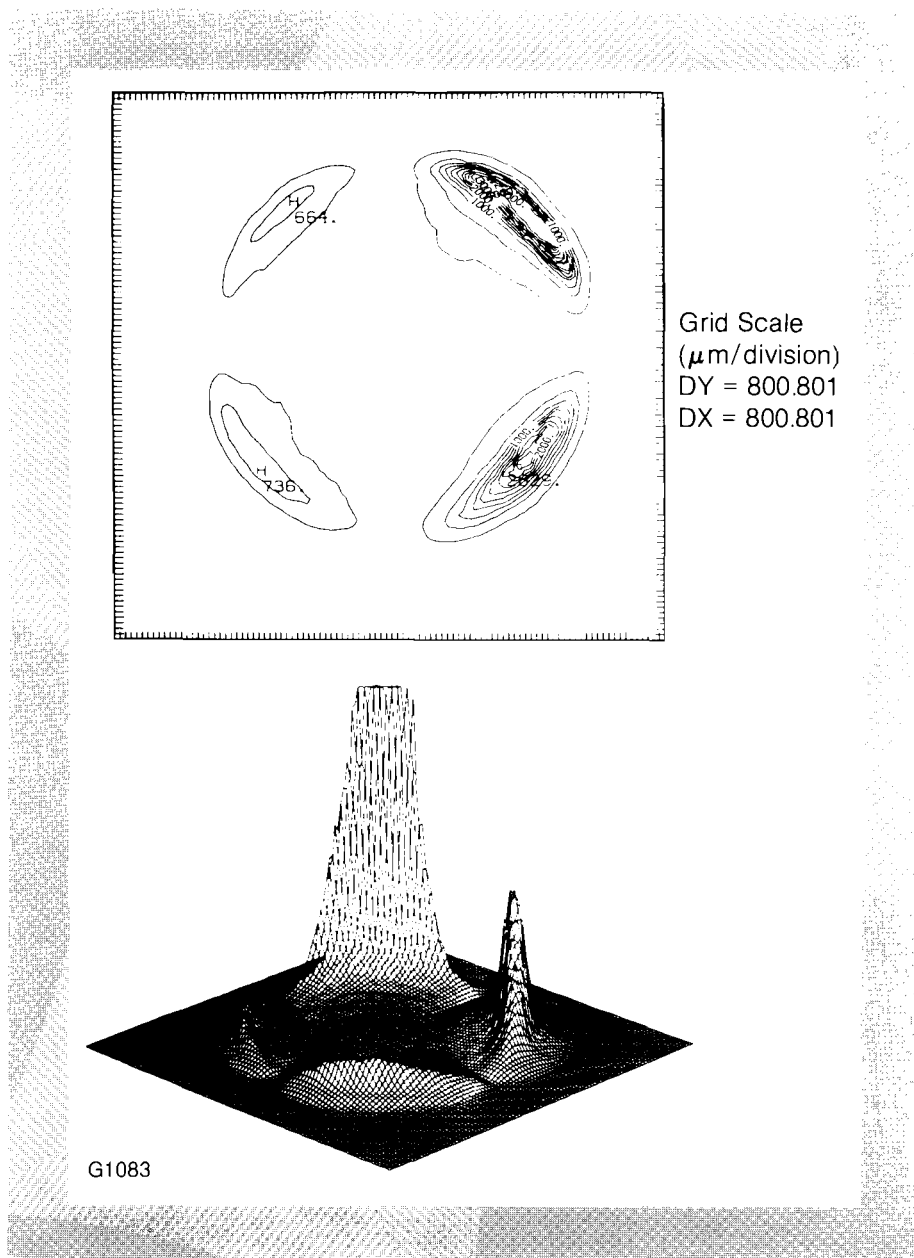
Grid Scale
(μm/division)
DY = 800.801
DX = 800.801

G1083

Fig. 22
Intensity distribution from the original OMEGA driver line with the throttle plate axis set at 45° to the vertical.

The second example illustrating the importance of thermal birefringence, is from a series of characterization shots performed on the system in early 1981.[3] In this particular test, the system was fired 13 times at a twelve-minute repetition rate. (Note that the system was designed to have a minimum time between shots of 30 minutes.) The stage of interest is the "A" stage, after which the beam is split (by polarizing beam splitters) into four beams. The first "up/down" split of the four-way split is shown in Fig. 23. In all beam clusters, pure left-hand circularly polarized light is injected into the 64-mm rod. Ideally, this light has an azimuthally symmetric intensity profile. The 64-mm rod in this test exhibited an inverted temperature profile and was highly birefringent because of the relatively high repetition rate. The light emerging from the rod passes a quarter-wave plate aligned with its fast axis vertical. The light emerges with a spatially varying elliptical polarization but still with
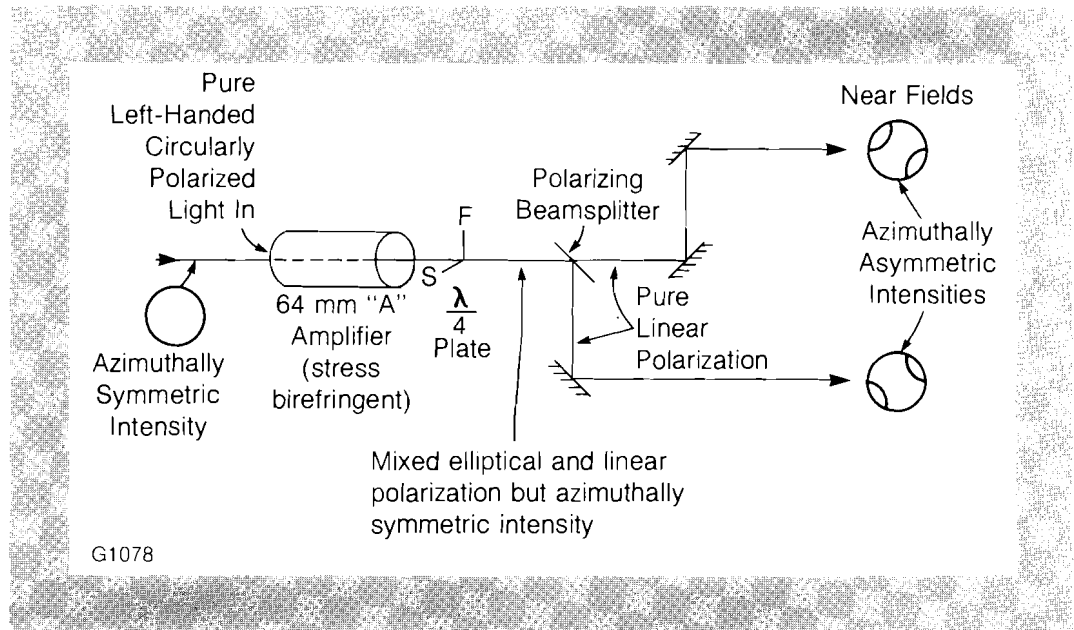
G1078

Fig. 23
Schematic layout of the OMEGA "up/down" beam-splitter system.

azimuthally symmetric intensity. If the emergent light were perfectly, linearly polarized, it would be split into identical, azimuthally symmetric beams. Since the polarization ellipses are actually distributed as shown in Fig. 24, the polarizing beam splitter splits the beam into two non-identical, non-azimuthally symmetric halves. The results of passing this beam through a vertically oriented polarizer is shown in Fig. 25. Again, the polarization ellipses (they are all straight lines) are shown. The orientation of all the lines are the same (having just passed a polarizer), but the lengths are different, indicating the relative transmission. The predicted profile of the beam includes suppression of the upper left and lower right quadrants. This is qualitatively what is observed as is shown in Fig. 26. (In Fig. 25, the beam is propagating out of the page. In Fig. 26, it is propagating into the page.) The exact beam shape will depend on the radial profile of the input beam and the temperature profile in the rod. No attempt was made to measure the birefringence of a 64-mm rod under high-repetition-rate conditions.

The lower beam is expected to be the mirror image of the upper. This is not quite what is observed, as is shown in Fig. 27. The beam has been diminished in the opposite quadrants, but significant modulation remains in the original upper left and lower right quadrants. It is not yet clear why this is, but a non-azimuthally symmetric input to the 64-mm rod is suspected.

As a result of this study, a change to circular polarization in the OMEGA driver line will be made in the near future. Work to identify other sources of azimuthal asymmetry in the system will also continue. The measured values of stress birefringence have been incorporated into the raytrace code *RAINBOW* and are being used to predict losses at polarizers.

Fig. 24
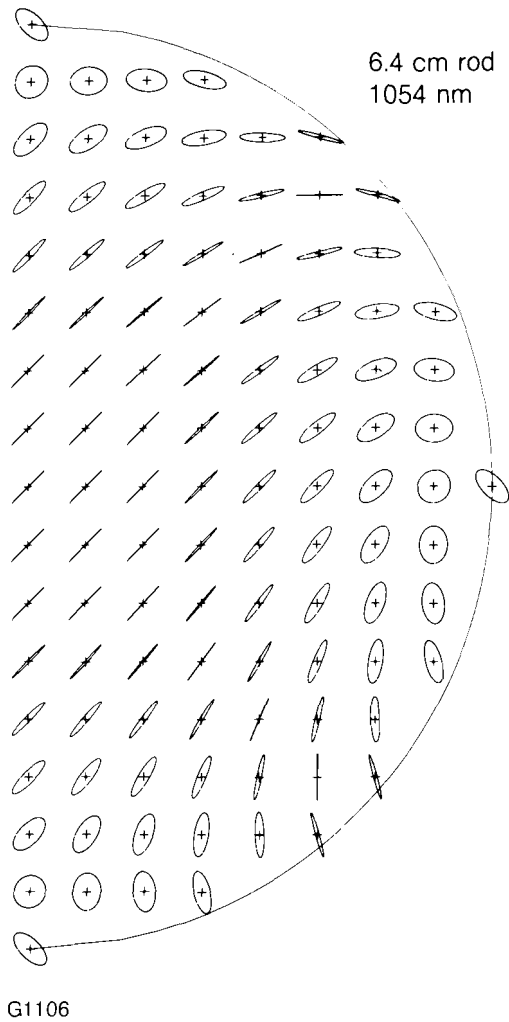Spatial distribution of polarization measured immediately after the quarter-wave plate in the "up/down" beam-splitter system (Fig. 23).
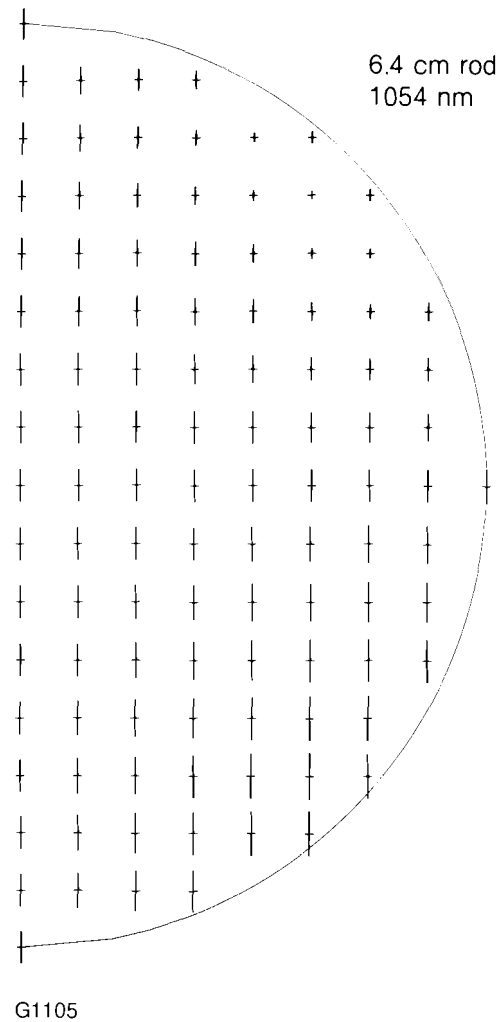
Fig. 25
Spatial distribution of polarization measured after the vertical polarizer in the "up/down" beam-splitter system (Fig. 23).

REFERENCES

1. S. Skupsky and K. Lee, LLE Report No. 137, January 1983.

2. F. W. Quelle, Appl. Opt. 5, 633 (1966).

3. LLE Review 7, 5 (1981).

G1085

Grid Scale
(mm/division)
DY = 2.165
DX = 2.165

Fig. 26
*Isointensity contour plot of the intensity
distribution of the upper beam from the
"up/down" beam-splitter system (Fig. 23).
This pattern was recorded after firing 13
shots on the OMEGA system at a 12-min-
ute-repetition rate.*

G1084

Grid Scale
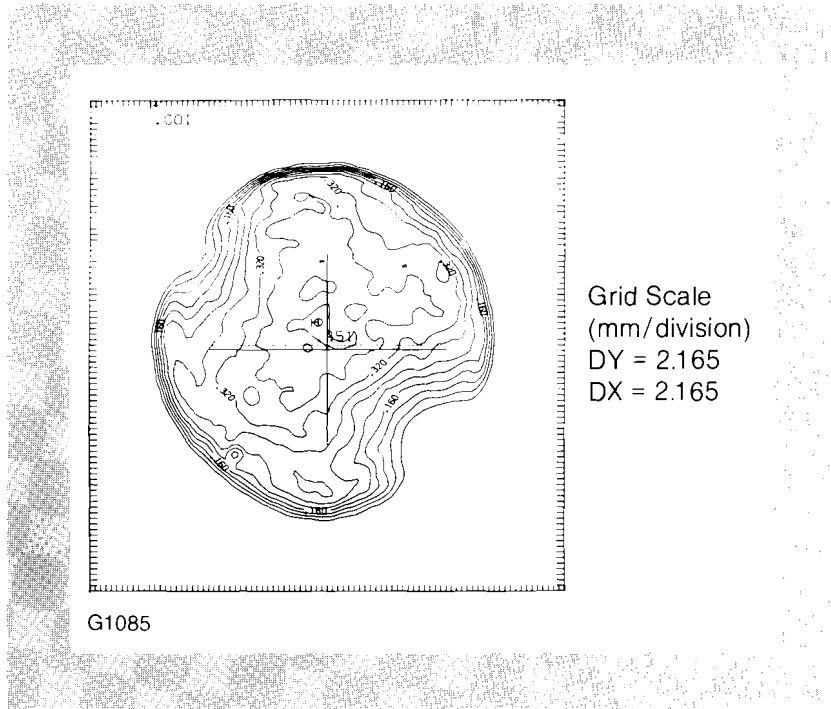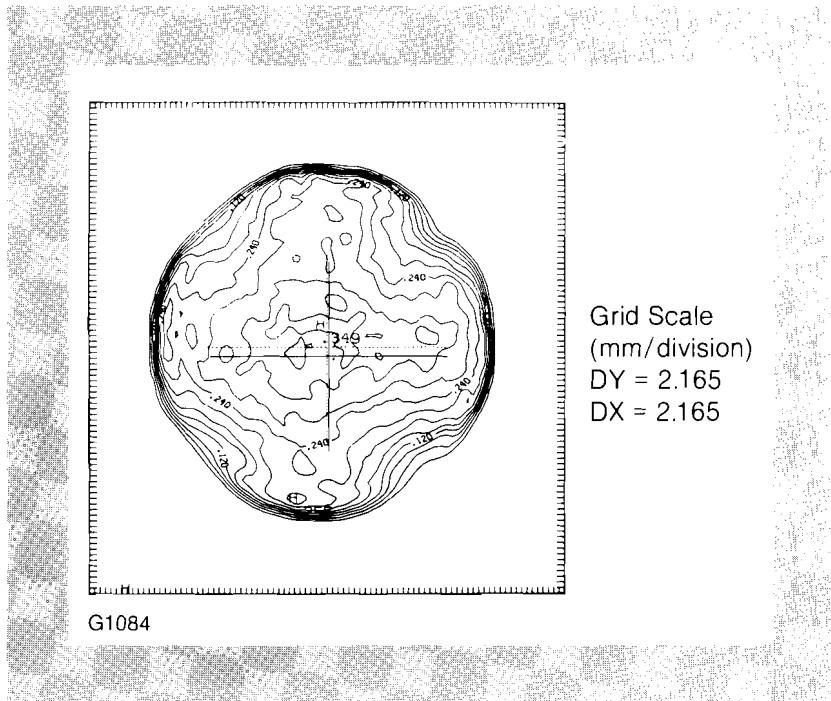(mm/division)
DY = 2.165
DX = 2.165

Fig. 27
*Isointensity contour plot of the intensity
distribution of the lower beam from the
"up/down" beam-splitter system recorded
at the same time as the pattern shown in
Fig. 26.*

Section 3
DEVELOPMENTS IN
MICROFABRICATION

3.A Inertial Fusion Target-Mounting Methods: New Fabrication Procedures Reduce the Mounting Support Perturbation

Inertial fusion targets require a high degree of geometrical perfection for optimum, fusion-implosion performance. Theoretical design considerations establish exacting specifications for target fuel-core sphericity, target layer-thickness uniformity, and target surface smoothness for calculated fuel compressions. Recent target fabrication activities have concentrated on developing processes capable of both producing and verifying these exacting specifications. This section reports on research aimed at minimizing the geometrical imperfection caused by the use of fusion target delivery supports.

Current laser-fusion target delivery systems use thin fibers or films to support and position the target at the focal volume of the irradiation system. Using current procedures (100-μm-diameter x 1-μm-wall glass microballoon bonded on a 10-μm-diameter glass fiber, for example), the constituting support mass introduced into the implosion dynamics is often a substantial fraction of the total target mass—a significant contribution to target asymmetry. The critical requirements for target delivery have been examined with the goal of identifying and developing techniques which (1) minimize the adverse effects of the support on target performance through geometry and material selection, (2) have application to the range of targets currently of interest in the fusion program, (3) can be implemented without major modification of target chamber engineering, and (4) have an acceptably low rate of target delivery loss. Target injection or levitation system schemes do not meet these requirements.[1] We have developed two new target delivery sys-

tems, based on mechanical supports, that have reduced the effective target support mass by a factor of 1000 below usual values and that have produced demonstrated improvements in target implosion symmetry.

Target delivery supports influence implosion performance through (1) the asymmetry introduced by the support and (2) the material mismatch between the support and the outer target surface. These two considerations establish guidelines, listed below, for improving target delivery systems. For asymmetry, the effective support mass (the target support material that is within a distance ℓ of the target surface) can influence the implosion dynamics. For material mismatch, support material having an atomic number different from the material of the target surface can give rise to magnetic fields which can affect implosion dynamics.

Two representative target delivery support systems commonly used are the fiber and the film mount. The fiber support material has usually been a drawn glass capillary or short silica, carbon, boron, or polymer filament adhesively bonded to the target. The film material has usually been formvar. Figure 28 shows the relationship between the effective
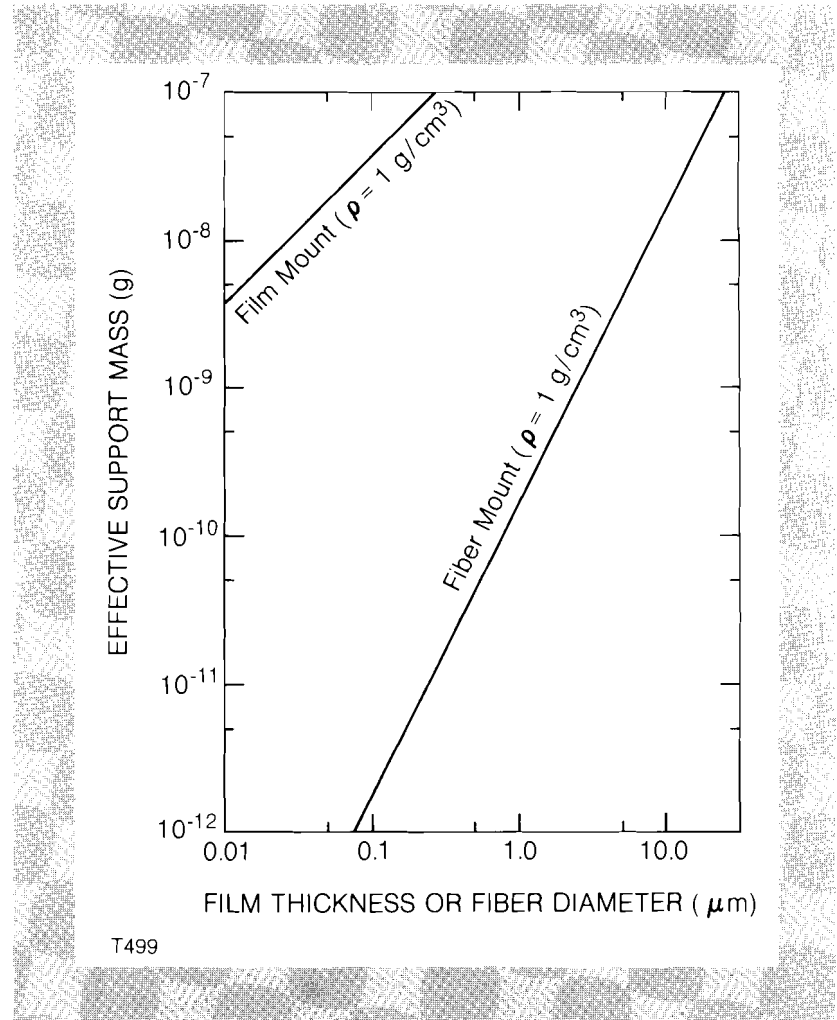

Fig. 28
Relationship between effective target-support mass and support dimension. The material densities of the film and the fiber are 1 g/cm³, the target diameter is 400 μm, and support influence range is 200 μm.

29

support mass introduced by each delivery system and the nominal support dimensions. Here d is the fiber diameter or the film thickness. These calculations are based on a 400-μm-diameter target, an assumed support influence range of $\ell = 200\,\mu$m, a support material density of 1 g/cm^3, and no added mass from adhesive material used to attach the target to the support. Nominal dimension values reported in the literature for these two target delivery systems are fiber diameters $\geq 10\,\mu$m and film thicknesses $\geq 0.01\,\mu$m. As Fig. 28 demonstrates, comparable effective support masses result with a 100-Å-thick formvar film ($\rho = 1$ g/cm^3) and a 3.5-μm-diameter glass fiber ($\rho = 2.5$ g/cm^3). For reference in this figure, a 100-μm-diameter x 1-μm-wall glass balloon has a mass of 8x10^{-8} g.

The slope of the fiber support curve in Fig. 28 is larger than that of the film support curve, indicating that greater reduction in target delivery support mass is achievable through reducing fiber rather than film dimensions. Target delivery systems based on film supports were not pursued for this technical reason. The next two sections describe procedures developed to fabricate and use micrometer and submicrometer diameter fibers to support and position fusion targets for irradiation experiments. Reported delivery reliability results are based on successfully positioning the target in the laser focal volume, evacuating the target chamber, and irradiating the target.

Two approaches were investigated for fabricating glass-fiber target supports. The first involved mounting the target on commercially available glass-fiber material using standard techniques.[2] Single fibers from Johns-Manville Tempstran glass wool[3] having diameters in the range of 0.3 to 5 μm and lengths of approximately 1 cm were removed with forceps. One end of a fiber was bonded to a drawn glass capillary using UV curing epoxy. The free end was then either butt-mounted or tangentially mounted to the target surface using the same adhesive. Selecting, extracting, and handling individual fibers, performed with a stereo-microscope in previous target assemblies, proved difficult because of limited optical resolution. Practical handling considerations placed a lower limit of 2-μm diameter for this approach. Delivery reliability for ≤ 4-μm-diameter butt mounts was unacceptably low, but nearly 100% for tangential mounts made with 2- to 4-μm-diameter fibers. Another advantage, in addition to size, of these tangential fiber mounts over conventional drawn capillary butt mounts is the uniform cross-section of the fibers. Drawn capillaries with a 10-μm-diameter tip typically have a 3° taper, causing a 20-μm diameter at the 200-μm distance and giving a correspondingly effective mass increase.

The second glass-fiber target delivery system involved adhesively bonding a target to a fiber formed by performing additional drawing steps on conventional glass capillaries. This method, adapted from a technique developed by E. Diacumakos,[4] circumvents the previously described fiber-handling difficulties. In brief, 1.5-mm-diameter glass capillary tubing is pulled to a tapered point using a micropipette puller. Viewing the operation through a 320-power, long-working-distance compound microscope, the point is pressed into a heated 0.25-mm-diameter Nichrome wire to form a molten glass bead ∿0.1 mm in size.

With the wire still heated, the capillary tube is retracted 5 mm at a rate of 1 mm/s, causing glass material to be drawn from the molten bead to form a thin, constant-cross-section glass fiber. Current to the wire is then turned off. Further retraction of the capillary tube fractures the thin fiber, usually at the surface of the glass bead. This fiber fabrication process reproducibly forms fibers in the range of 0.75 to 1.5 μm in diameter.

Adhesively butt-mounting the produced fibers is difficult because of the small contact area present at the fiber tip, but reliable tangential mounts have been formed. However, a procedure for forming a 90° bend at the tip of the thin fiber has been developed; the bend provides increased adhesive contact area that allows formation of a reliable butt mount. This procedure involves pressing the thin glass fiber into the room temperature wire until noticable deflection is evident near the tip. Current is applied to the wire to raise the fiber temperature to the glass softening point, causing a 90° bend to form near the fiber end. The bent section is usually 20 to 50μm in length. Laser trimming of the fiber to a 10-μm length follows. Fiber attachment to the wire usually does not occur if the wire temperature is kept at a minimum. Figure 29 is a micrograph of a 400-μm-diameter target supported on a 0.8-μm-diameter bent fiber.

400 μm

T520

Fig. 29
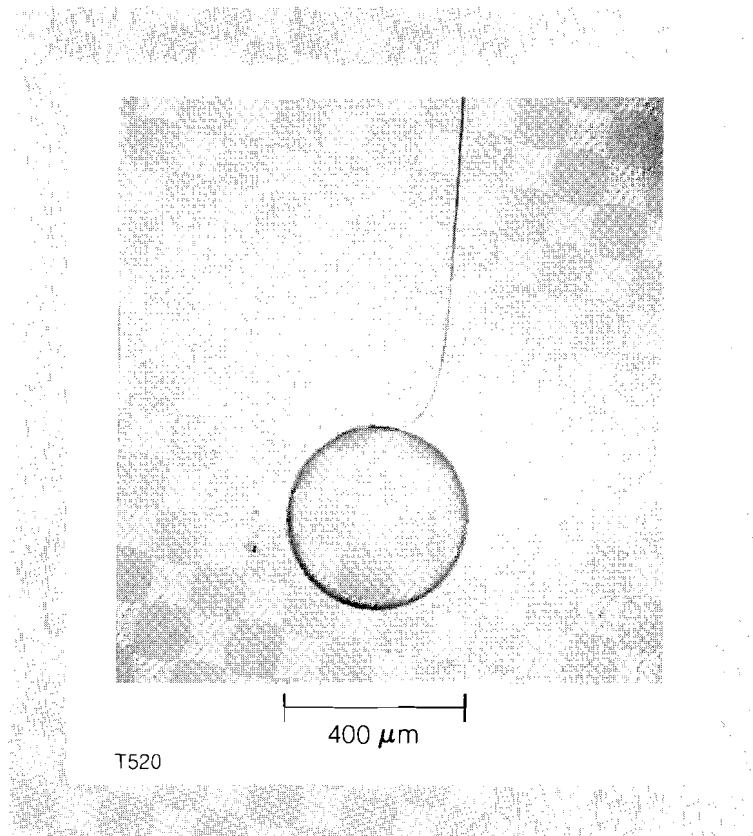*SEM micrograph of fusion target supported with a drawn glass fiber.*

Special efforts were required to apply correspondingly small quantities of adhesive on the thin glass fibers. Dow Corning Z-6040 silane coupling agent was found to assist adhesive applications to the small fibers. The silane pretreatment included dipping the fiber tips in a 0.25% aqueous silane solution, followed by oven drying. This provided contin-

uous adhesive coverage rather than discrete adhesive droplet formation. Adhesive materials tested and found adequate included Devcon "5-minute" epoxy and Dow Corning 734 RTV self-leveling adhesive/sealant. The preferred adhesive material is the epoxy because curing occurs within an hour at room temperature. The RTV, in the quantities used, required a considerably longer curing time. The UV epoxy did not cure. Delivery reliability for glass fibers in the diameter range of 0.75 to 1.5 μm was approximately 90%.

Fig. 30
Silk-fiber, target-mounting sequence. Single silk fibers are extracted (a), positioned in an assembly fixture (b), bonded to a fusion target (c), bonded to a drawn glass capillary (d), and shortened to the desired length (e).

(a)

(b)

(c)

(d)

(e)

T475
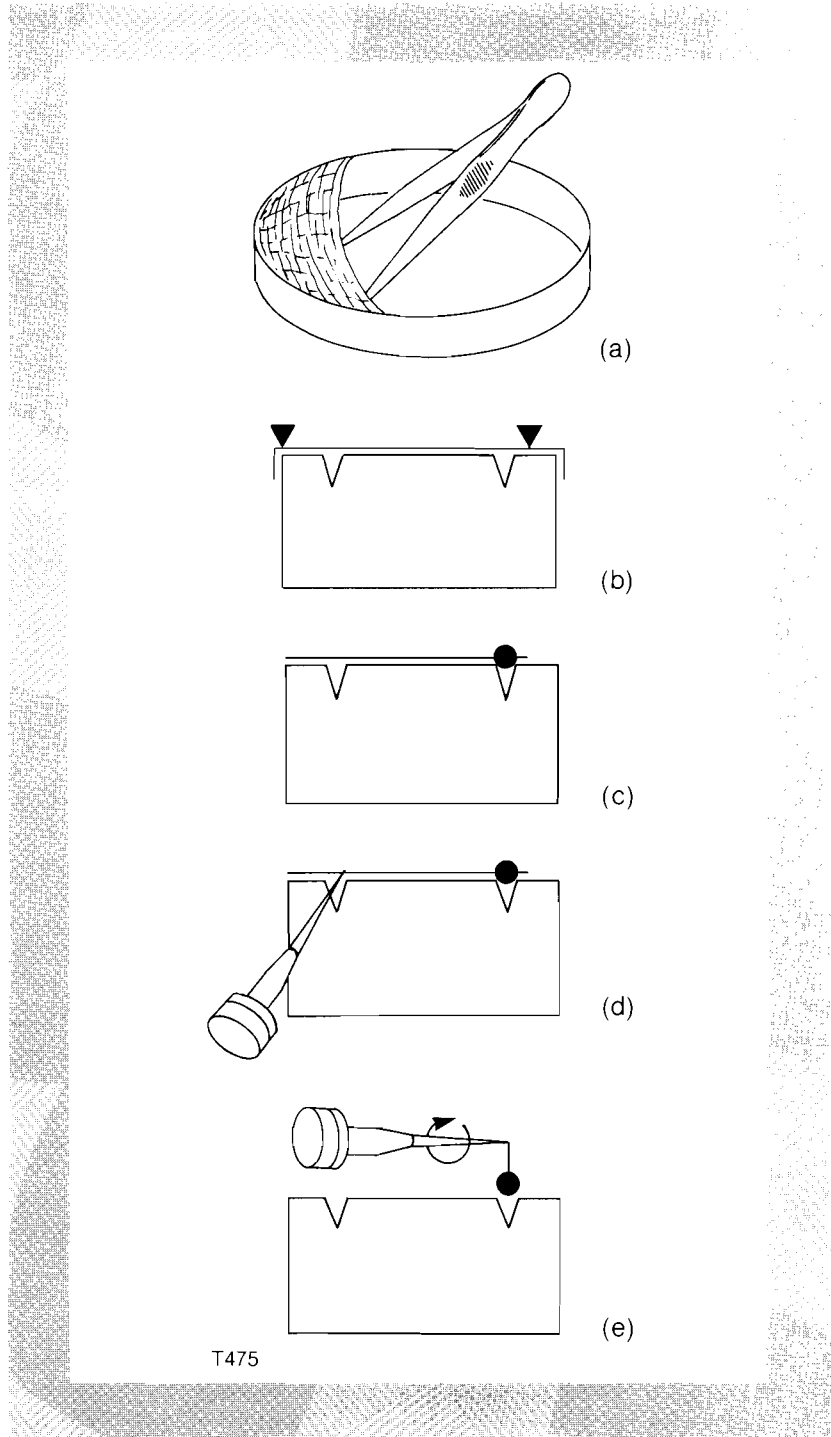
Polymeric fiber, target-support material, in addition to having a density lower than that of glass, better matches the average atomic number of the outer ablative target surface. Because a commercial source of submicron polymeric fibers was not located, spider silk, a polymerized scleroprotein, was investigated with regard to its suitability for target delivery supports. One type of silk, viscid Ecribellatae web material,[5] has been found to be extremely well suited for this application. The material is strong, is available in the diameter range of interest, and is coated with a natural adhesive. Two target-mounting procedures have been developed to reliably support fusion targets on submicrometer-diameter silk fibers for irradiation experiments.

The first assembly procedure produces a target that hangs vertically on a single 300- to 500-μm-long, 0.2- to 0.5-μm-diameter silk fiber. Assembly steps include positioning a silk strand on an assembly fixture, then attaching the target to one end and a drawn glass capillary to the other end. As illustrated in Fig. 30a, single silk strands are extracted with open tweezers from the edges of webs built in petri dishes containing a single Ecribellatae. The open tweezers are then positioned over a flat black aluminum assembly fixture, and the fiber is cut on both fixture sides with a razor to transfer the silk, as shown in Fig. 30b. A fusion target is positioned with a vacuum chuck into one of the 200-μm-deep vee grooves so that contact is made with the fiber (Fig. 30c). This step usually requires some fixture rotation under a side-illuminated stereo microscope to make the fiber visible. Silk material extending outside of the 3-mm separated parallel vee grooves is then cut. The point of a drawn glass capillary previously loaded into a magnetic target chamber positioner base is then contacted to the fiber in the second vee groove (Fig. 30d). Vertical motion of the horizontally oriented glass capillary causes separation of the fiber-mounted target from the assembly fixture (Fig. 30e). If initial fiber adhesion does not occur, repeated attempts usually produce bonding. The capillary is then rotated, causing fiber winding at the capillary tip, until the target-capillary separation distance is ~300 to 500 μm. The target-fiber adhesive contact is shown in the Fig. 31 SEM photograph. Precautions found necessary for successful completion of the procedure include shielding all described activities from air currents (including the operator's breathing), and maintaining a vertical target-capillary orientation after the fiber-shortening step is completed to prevent target-capillary attachment. Delivery reliability for single 0.25- to 0.5-μm-diameter silk was greater than 75%.

The second assembly procedure, a variation of the ring-mounting technique commonly used to support the fuel core in colliding shell targets, provides significant effective mass reduction over previously reported polymer films and fibers.[6,7] Here, two fibers are positioned across a target-mounting ring or hemispherical shell. Excess silk material is then removed, and the target fuel core is placed between the separated fibers using a vacuum chuck. Figure 32 is an SEM photograph of a glass microballoon mounted in this configuration. Here the fiber diameters are approximately 0.4 μm, and the microballoon diameter is 400 μm. Solid steel ball bearings 500 μm in diameter have been reliably mounted and delivered with this procedure, an indication of the strength and surface adhesion of viscid Ecribellatae silk.
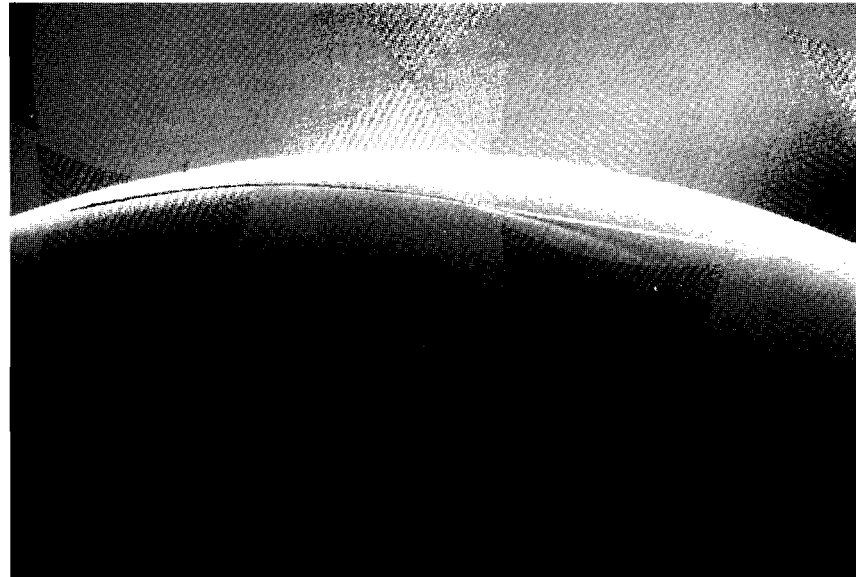
T494

10 μm

Fig. 31 SEM micrograph of fusion target showing viscid Ecribellatae silk adhesive contact area.
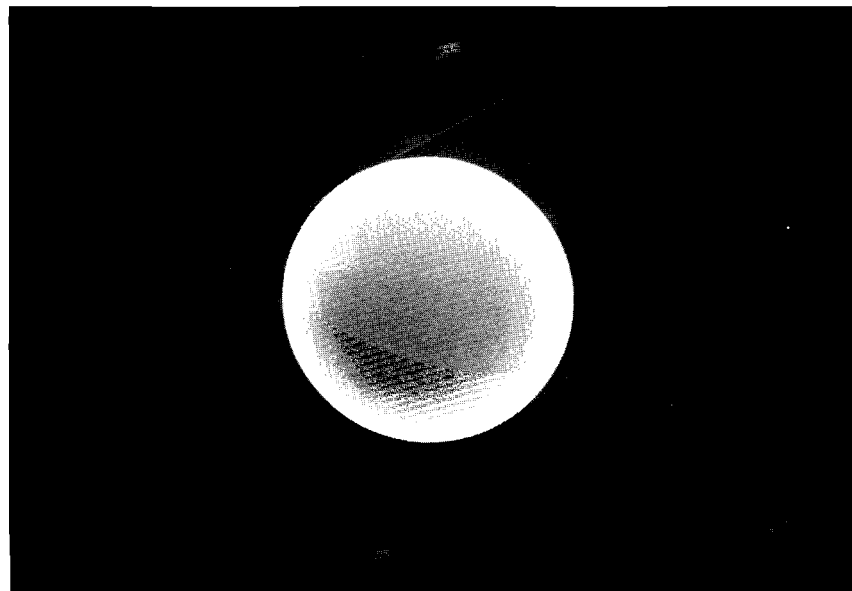

T518

400 μm

Fig. 32 Fusion target fuel core-mounted using two silk fibers in the geometry of a colliding shell target.

In both assembly procedures, no adhesive application was required for supporting targets using viscid Ecribellatae silk. The natural "sticky" silk surface was sufficient for reliable bonding.

Improved implosion symmetry has been demonstrated using the new support methods. Soft x-ray pinhole images produced by two comparison targets that were irradiated under similar conditions, along with target micrographs, are shown in Fig. 33.[9] Figure 33a shows a target mounted using a conventional drawn glass capillary. The corresponding pinhole image (Fig. 33c), shows marked asymmetry near the stalk. The newly developed viscid silk mount (Fig. 33b) permitted a more symmetric implosion (Fig. 33d). No stalk perturbation is evident here. Similar improvements have been found using the submicrometer glass-fiber mounts.

Fig. 33
Comparison target micrographs and x-ray implosion images.
  a) Conventional drawn glass capillary mount
  b) Viscid Ecribellatae silk mount
  c) Soft x-ray pinhole image produced by (a)
  d) Soft x-ray pinhole image produced by (b)

(a)

(b)

400 μm

(c)

(d)

400 μm

T521

35
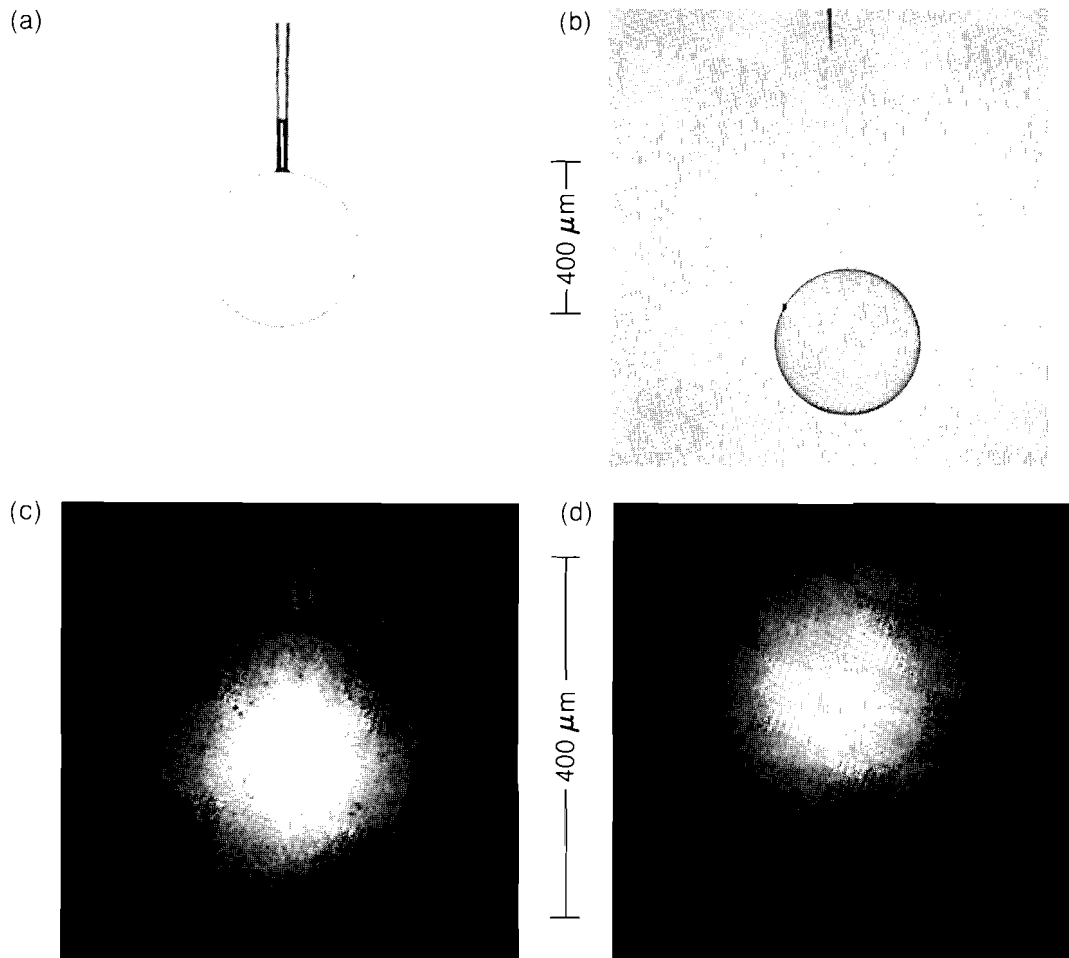
Minimum effective support mass was achieved using single 0.25-μm-diameter viscid Ecribellatae silk having an estimated density of 1.2 g/cm.³ This material closely matches the average atomic number of target ablation layers and does not require adhesive application for target bonding, an important practical advantage. Drawn glass fibers with diameters ≥0.75 μm have been reproducibly fabricated and have been shown to reliably support targets for irradiation experiments. This type of fiber has a higher density (2.5 g/cm³) than the silk material and does require adhesive application. Commercial glass fibers, even though available down to 0.3 μm in diameter, presented practical difficulties that were not overcome for diameters less than 2μm. Although target delivery will ultimately involve nonmechanical supports, the new mounting developments reported here are expected to postpone the need for conducting irradiation experiments with injected or levitated targets.

REFERENCES

1. The following papers describe various nonmechanical delivery approaches. Each approach would require considerable hardware development and refinement before implementation in our 24-laser-beam target chamber.

     J. L. Pack, T. V. George, and A. G. Englehardt, *Rev. Sci. Instrum.* **39**, 1697 (1968).

     D. B. VanHulsteyn and L. Anderson, *Rev. Sci. Instrum.* **44**, 453 (1973).

     D. Burgeson, KMS Fusion, Inc., Annual Report (1978).

     S. L. Milora, G. A. Foster, D. H. Edmonds, and G. L. Schmidt, *Phys. Rev. Lett.* **42**, 97 (1979).

2. B. Cranfill, E. H. Farnum, A. T. Lowe, and J. R. Miller, *Technical Digest of Topical Meeting on Inertial Confinement Fusion* (Optical Society of America, Washington, DC, 1978), Report ThE 2-1.

3. The source for this material was suggested by D. Steinman.

4. E. G. Diacumakos, "Methods for Micromanipulation of Human Somatic Cells in Culture," in *Methods in Cell Biology*, edited by David M. Prescott (Academic Press, New York, 1973), Chap. 15, pp. 290-296.

5. B. J. Kaston, *Natur. Hist.* **75**, 27 (1966).

6. Ye. G. Gamilii, A. I. Gromov, A. I. Isakov, L. A. Krupinina, Yu. S. Leonov, F. I. Matveeva, Yu. A. Merkul'ev, A. I. Nikienko, Ye. R. Rychkova, and G. V. Sklizkov, Akademiia Nauk SSSR, *Fizicheskii Institute Imeni P. N. Lebedev, Trudy* **94**, 29-60 (1977) (Translated-LA-TR-78-21).

7. *Inertial Fusion Program, Progress Report, 1 January-30 June 1978*, L-7587-PR, Los Alamos Scientific Laboratory (May 1980), pp. 146-147.

8. D. J. Borror, D. M. DeLong, and C. A. Triplehorn, *An Introduction to the Study of Insects* (Holt, Rinehart, Winston, 1976), pp. 94-121.

9. M. C. Richardson and D. M. Villeneuve, Laboratory for Laser Energetics, University of Rochester, unpublished data, 1982.

3.B Progress in Biased Magnetron Sputtering of ICF Target Pusher Layers

Hollow glass microballoons (GMB's) which are fractions of a millimeter in diameter are often used as fuel pellets in laser fusion experiments. Many designs require metal coatings whose thicknesses and densities vary by less than a few percent throughout the coating, and whose surface roughnesses are 50 nm or less. Applying these coatings to GMB's by means of sputtering or evaporation poses a unique set of challenges, not the least of which is the inherently oblique incidence of the coating flux. This typically leads to columnar growth defects, and a rough surface morphology.[1] Substrate bias has been studied extensively as a means of controlling the properties of sputtered coatings,[2] but we are unaware of any published work reporting the use of bias in coating GMB's.

The effect of substrate bias in the case of metal coatings on GMB's is interesting for several reasons. One method which has been proposed for coating unsupported GMB's is electrostatic levitation,[3] requiring a rather large charge on the substrate. It is important that the influence of this charge be understood. In addition, molecular beam levitation has been used for unsupported GMB coatings[4-6], and the effects of the self-bias acquired during sputtering are of interest. It has been suggested that this self-bias can lead to surface roughening.[6]

In an earlier report,[7] we described the effect of substrate bias on Ni coatings sputtered onto hollow glass microballoons. We have extended this work to examine bias-sputtered copper and aluminum on planar as well as spherical substrates. We have also studied the coating environment with Langmuir probes, and propose a model in which enhanced normal incidence of the coating flux is responsible for improved film microstructure.

The vacuum system and charging circuit have been described previously.[7] A total of 21 GMB's with diameters ranging from 190 μm to 570 μm have been coated in tests to date. Of these, 14 were done with bias and 7 without bias. For comparison, two planar substrates 2 cm x 2 cm were coated with Cu, one at 0-V bias and the other at $-$ 100-V bias. They were positioned at the same location as the microballoons with their planes normal to the source axis.

In order to determine the plasma characteristics at the location of the GMB's, a conducting cylinder 1.50 mm in diameter was used as a Langmuir probe. The current-voltage characteristics of the probe were measured for applied voltages from $-$ 10 V to $+$ 50 V while sputtering Cu at a current of 1.0 A and pressure of 1.3 Pa.

As reported earlier,[7] all of the GMB's coated without bias exhibited surface structure which is characteristic of columnar growth due to oblique incidence of the coating flux. Several representative samples were fractured, and the coating cross sections were viewed with an SEM. The coating thicknesses on unbiased GMB's were uniform within

an uncertainty of 5%, as determined from measurements made at several points on each fractured unbiased GMB. Furthermore, the coating morphology was the same everywhere on any individual unbiased GMB.

Substrate bias produced a general overall improvement in coating microstructure and surface smoothness, and the results were qualitatively the same for all three metals. The structure of a typical biased coating depended on the position on the GMB surface. If we denote the point where the stalk joined the GMB as the south pole, and the diametrically opposite point the north pole, the coating microstructure and surface smoothness of biased GMB's were always best at the north pole. Figure 34a is a photomicrograph of an unbiased Ni coating, and Figs. 34b and 34c are respectively the north and south poles of a GMB coated with Ni using a bias of − 100 V. The texture and surface smoothness have improved as a result of bias, with improvement at the north pole being considerably better than the south pole. The improvement due to bias was found to scale with the applied voltage.

Generally, the biased coatings were far more ductile than the unbiased coatings, causing them to pull apart rather than fracture. This made it difficult to measure accurately the film thicknesses for the biased coatings. In those cases where measurements of thickness could reasonably be made, however, the accumulation rate at the north pole
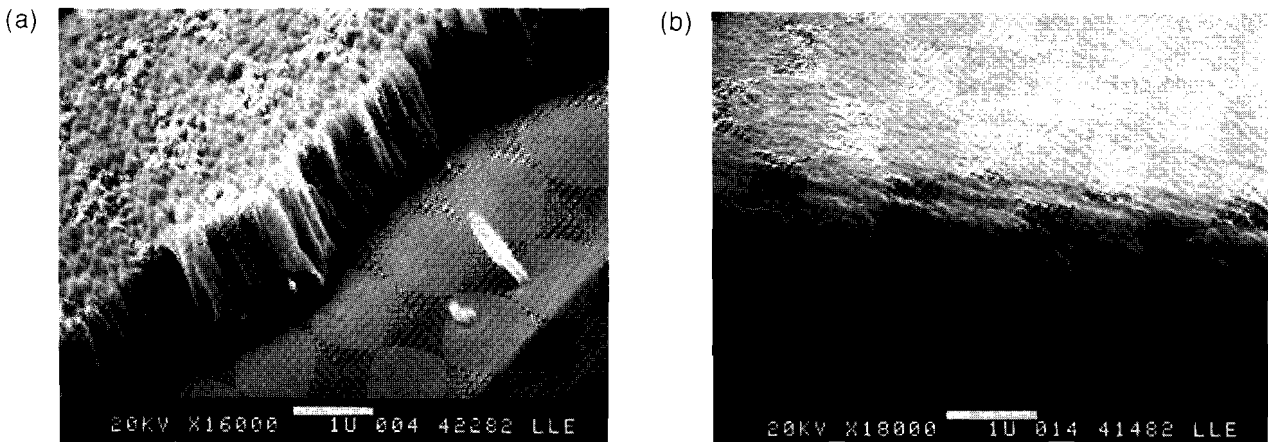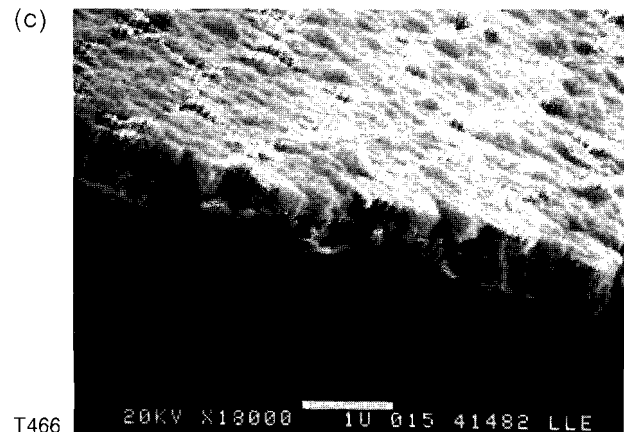
(a)

(b)

Fig. 34
Comparison of Ni coatings on an unbiased
GMB (a) with north pole (b) and south pole
(c) of a GMB biased at − 100 V.

(c)

T466

was greater than that at the south pole. This can be seen by comparing Figs. 34b and 34c. This variation in thickness was only observed in the case of biased GMB's.
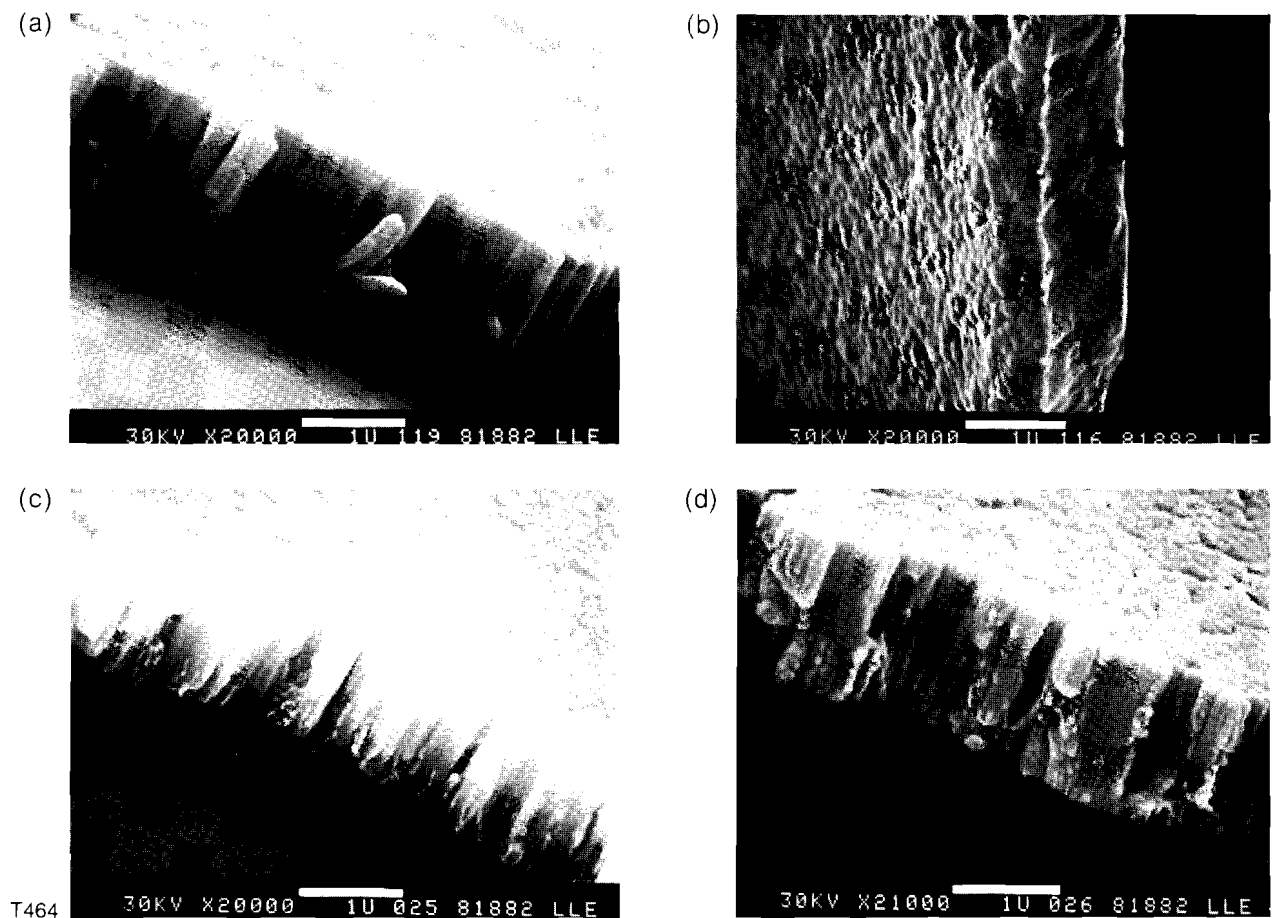
The importance of substrate geometry is illustrated in Fig. 35. Figure 35a is a Cu coating applied to an unbiased GMB, while Fig. 35b is Cu which was coated on a GMB biased at − 100 V. A clear improvement is seen with bias. By contrast, Figs. 35c and 35d are Cu coatings applied under otherwise identical conditions to planar substrates which were unbiased and biased at − 100 V respectively. No clear improvement is evident as a result of bias for the planar substrates.

Based on the Langmuir probe measurements, the plasma density at the substrate was found to be approximately $5 \times 10^9/cm^3$. The electron energy distribution was non-Maxwellian, but an average temperature of 0.5 eV was calculated.[8,9]

Fig. 35
Comparison of the effect of bias on GMB's with the effect of bias on planar substrates. (a) and (b) are Cu coatings on GMB's biased at 0 V and − 100 V respectively, while (c) and (d) are Cu coatings on planar substrates biased at 0 V and − 100 V respectively.

Resputtering during film growth is the explanation often given for the results of biased sputtering, although this is a simple way of describing a very complex process.[2] The nature of the ion bombardment of the substrate in our case is determined by the sheath which surrounds the stalk/GMB. If we assume that ions enter the sheath with thermal velocities, ions of a particular species which arrive at a given location on the GMB will have a single velocity which is determined by the electric field sur-

(a)

(b)

(c)

T464

(d)

rounding the GMB. By symmetry, at the north pole this velocity will be normal to the surface of the GMB, while at the south pole the stalk, with a diameter approximately 10% that of the microballoon, will produce a perturbation which results in non-normal ion incidence. It is possible that this non-normal incidence, which would be expected to lead to higher resputtering yields, may account for the generally lower rate of accumulation at the south pole. However, if resputtering were the only mechanism responsible for the improvement in coating quality, we would expect the thinner portion of the coating to be smoother and denser than the thicker portion, which is not the case.

It is possible that metal ions in the plasma may play an important role in our coatings. Even though they account for a small percentage of the metal vapor, the spherical geometry of our substrates will increase their significance. To illustrate, we will consider a GMB of radius r_G which is surrounded by a sheath of radius r_s. Since essentially all of the ions which enter the sheath will strike the substrate, the ratio of the effective area of the substrate for ions to that for neutrals is $(r_s/r_G)^2$. If a fraction γ of the metal vapor is ionized, then the ratio of the metal ion flux to the metal neutral flux is given by $\gamma(r_s/r_G)^2$. Consequently, for GMB's surrounded by sheaths several times their radii, the metal ion flux may play an important role in the coating process, even for small values of γ. This is particularly true when we consider that the metal ions will arrive at near normal incidence at the north pole, which may help explain the significant improvement at this location.

We can estimate the sheath radius in our experiments from the Langmuir probe data to be approximately 2 mm. The mean free path at our pressures is approximately 1 cm, making collisions in the sheath unlikely. This estimate is, of course, voltage dependent, and will certainly be different from stalk-mounted GMB's. Nevertheless, it indicates that for GMB's fractions of a millimeter in radius, the ion flux at the substrate could be enhanced by as much as two orders of magnitude.

The results of the experiments with planar substrates support the proposed explanation. In a planar geometry, a sheath whose thickness is small compared to the substrate dimensions will not alter the ratio of metal ions to metal neutrals striking the substrate, when compared to the unbiased case. Thus, we would expect little change as a result of bias other than that due to resputtering.

We therefore conclude that, in addition to resputtering, enhanced metal-ion bombardment as a result of bias contributes to the improvement in film structure which we have seen. This enhancement occurs because of the relatively large plasma sheath which surrounds the GMB's, producing a sizable number of metal ions arriving normal to the substrate. The reduced effect of bias in the case of planar substrates supports this conclusion. It is encouraging that large substrate biases appear to improve the quality of metal coatings sputtered onto GMB's. This provides an added bonus in the use of electrostatic and electrodynamic levitation schemes for unsupported GMB coatings.

REFERENCES

1. S. F. Meyer, *J. Vac. Sci. Technol.* **18**, 1198 (1981).

2. A summary of this technique, with references, is given by Brian Chapman, *Glow Discharge Processes* (John Wiley & Sons, New York, 1980).

3. R. W. Weurker, H. Shelton, and R. V. Langmuir, *J. Appl. Phys.* **30**, 342 (1959).

4. A. T. Lowe and C. D. Hosford, *J. Vac. Sci. Technol.* **16**, 197 (1979).

5. J. K. Crane, R. D. Smith, W. L. Johnson, C. W. Jordon, S. A. Letts, G. R. Korbel, and R. M. Krenik, *J. Vac. Sci. Technol.* **20**, 129 (1982).

6. I. S. Goldstein, J. Varon, and P. J. McHugh, *J. Vac. Sci. Technol.* **20**, 1328 (1982).

7. *LLE Review* **10**, 25 (1982).

8. Francis F. Chen in *Plasma Diagnostic Techniques* edited by R. Huddlestone and S. Leonard (Academic Press, New York, 1965).

9. Irving Langmuir and Harold Mott-Smith, Jr., *General Electric Review* **27**, 449 (1924).

Section 4
NATIONAL LASER USERS FACILITY NEWS

This report covers the activities of the National Laser Users Facility (NLUF) during the quarter July to September 1982. During this period one user experiment was conducted on the GDL facility. This issue of the *LLE Review* highlights some of the results of this experiment conducted as a collaborative, UCLA/Yale University program. Participants in this experiment were Francis Chen, Chan Joshi, and Humberto Figueroa from UCLA; and Nizarali Ebrahim and Hiroshi Azechi from Yale University. During this quarter, the UCLA/Yale experiment accumulated 11 system shots (in previous quarters, 95 experimental shots plus 25 diagnostic check-out shots were dedicated to this experiment).

The objective of the UCLA/Yale experiment was to study the effects of parametric instabilities in producing energetic electrons and scattering of the incident laser light. In the underdense corona of a laser fusion pellet, two processes may occur which are of potential interest: the two-plasmon decay $(2\omega_p)$ instability and stimulated Raman scattering (SRS). Both of these processes can produce energetic electrons which can preheat the fuel before the pellet compresses. In the $2\omega_p$ decay instability, the incident laser light is converted into two plasma waves with a frequency matching condition of $\omega_o \approx 2\omega_p$, where ω_o is the incident laser frequency and ω_p the plasma wave frequency. The $2\omega_p$ instability can thus occur only at a point where the electron density is one-fourth of the critical density (n_c). SRS involves the conversion of the incident laser light wave into one plasma wave and scattered light wave. This process can occur for plasma densities $n < n_c/4$.

The experiments were conducted by first forming a sub-critical density plasma to eliminate the effects occurring at the critical density. A pre-pulse, with an energy of approximately 7 joules at 1.054 μm, was used to form the sub-critical density plasma. A second pulse, of approximately 35 joules at 0.35 μm, was then used to study the instabilities occurring in the underdense region. The critical density for 0.35 μm light is 9×10^{21} cm^{-3}. The spot size of the 1.054-μm beam was approximately 2 mm, producing an irradiance of 5×10^{11} W/cm^2. The 0.35-μm beam was tightly focused to a diameter of approximately 70 μm, yielding an irradiance of 10^{15} W/cm^2. The maximum plasma density was controlled by an appropriate choice of foil thickness. Carbon foils of 800 Å, 2000 Å, and 4000 Å were used as targets. Figure 36 shows a schematic of the experimental focusing conditions.
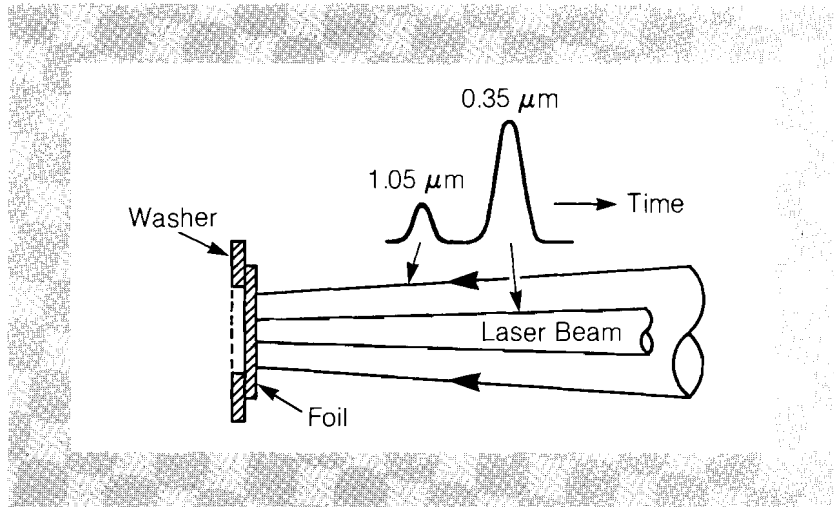

Fig. 36
Schematic of the experimental target set-up.

The diagnostics used in the experiments included two electron spectrometers to obtain the angular distribution of hot electrons between 35 and 350 keV. In addition, two visible spectrographs were used to obtain the Raman spectra backscattered through the focusing lens and at 45° to the lens. The backscattered spectrum was also temporally resolved using a subnanosecond-resolution streak camera. The data was then used to estimate the maximum density as a function of time. The side-scattered spectrum was spatially resolved to provide an estimate of the plasma density profile. Additional diagnostics, supplied by LLE, included six calibrated photodiodes to monitor the angular distribution of the $\omega_0/2$ light, an array of x-ray detectors to record the continuum spectrum, and a transmission calorimeter to obtain the transmitted 0.35-μm beam energy.

A summary of the observations from this experiment is shown in the following figures. Figure 37 shows an example of the time-integrated Raman backscatter. The spectrum is shown for three separate experiments with carbon foils of 800 Å, 2000 Å, and 4000 Å. In the long-wavelength region, the Raman spectrum extends up to 0.06 n_c for the thinnest foil. This density is observable because a specific wavelength of Raman scattering occurs at a specific density. Also, the data for the thinnest foil shows no half-harmonic emission at 0.7 μm. These observations imply that the thin-foil plasma density is less than $n_c/4$, at the time of the 0.35-μm laser pulse. When the target foil is increased in thickness, the Raman

spectrum extends to longer wavelengths and associated higher densities. The 2000 Å foil shows a cutoff corresponding to 0.09 n_c, while the 4000 Å foil shows a cutoff corresponding to 0.16 n_c. The harmonic emission at 0.7 μm is observed in both of the thicker foils, which is a unique signature that there is a $n_c/4$ density layer to interact with the 0.35-μm laser pulse. The results also show that the long-wavelength cutoff shifts as a function of foil thickness.
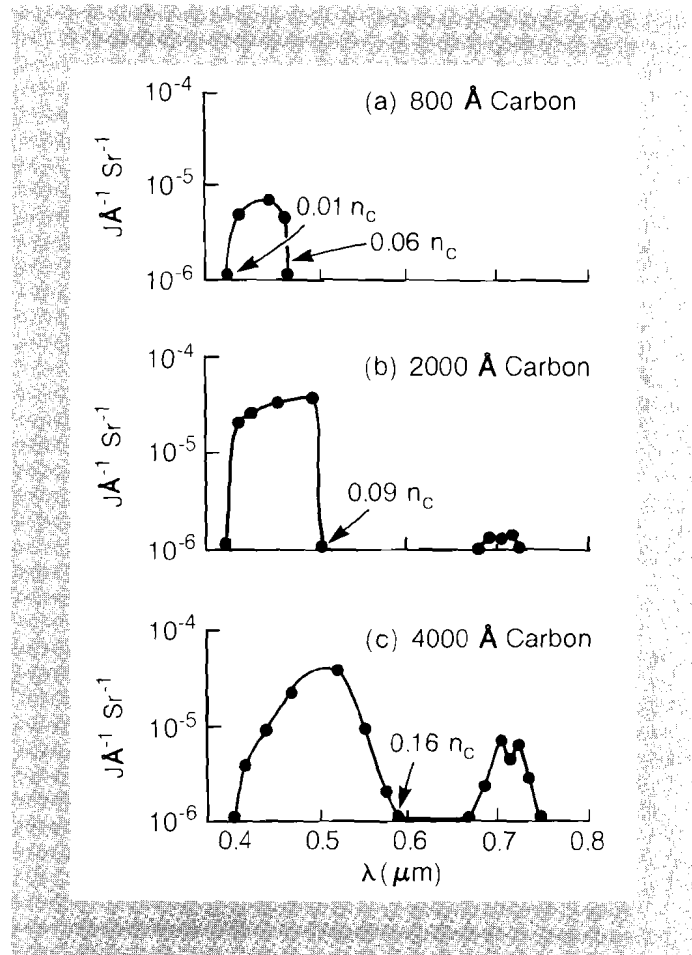

Fig. 37
Time-integrated Raman-backscatter spectra from carbon foils of various thicknesses.

An estimate of the temporally averaged density profile of the plasma was obtained by spatially resolving the 45°, Raman-sidescattered light. This density profile measurement is possible, because the Raman scattering from a specific density produces a specific wavelength. Raman-sidescattered light at 45°, with respect to the 0.35-μm beam, was imaged, using an achromatic lens, onto the slit of a 0.25-meter, space-resolving spectrograph. Information about the plasma was obtained between 0.075 n_c and 0.095 n_c for a 2000 Å carbon target. The plasma region between these densities was approximately 50 μm long.

An additional measurement of the time-resolved, Raman backscatter shows a shift of the long-wavelength cutoff to shorter wavelength as a function of time. An example of this effect for Raman-backscattered light from a 4000 Å carbon foil is shown in Fig. 38. Time is plotted on the vertical axis of Fig. 38 while wavelength (and its equivalent density) is plotted on the horizontal axis. The observed wavelength shift versus
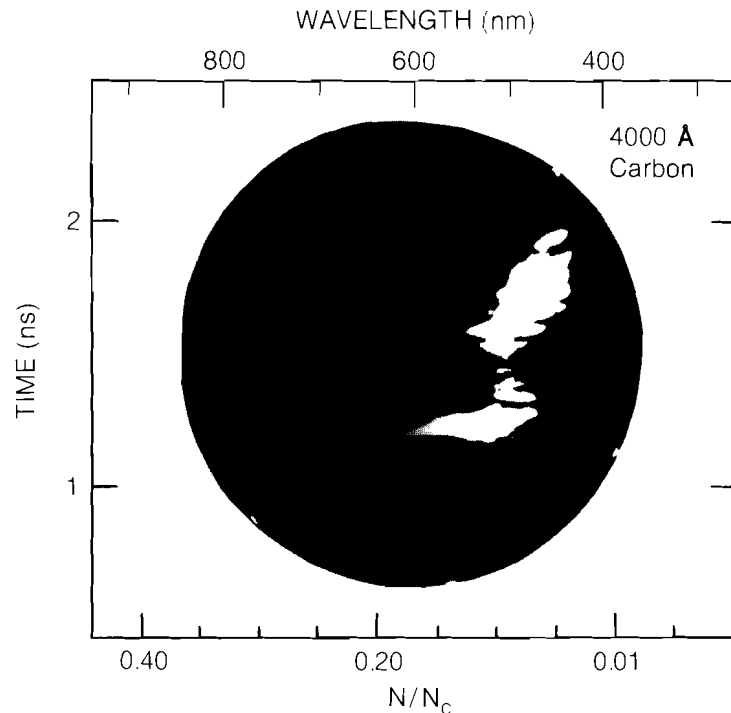
Fig. 38
A typical streak record of Raman-back-scattered light from a 4000- Å -thick carbon foil plasma.

time is indicative of the peak foil density (plateau region) decreasing with time. Still another measurement made use of the high-energy, electron emission associated with SRS and $2\omega_p$ instabilities. No significant electron emission was observed from the 800 Å foil plasma. The thicker foils produced readily observable high-energy electron emission. These measurements are consistent with high-energy electron generation at the $n_c/4$ density layer.

Additional information on these results can be obtained from the scientists associated with the experiment. The information on the UCLA/ Yale experiment is an excerpt from a UCLA report. This experiment was supported by a contract with the U.S. Department of Energy.

Future issues of the *LLE Review* will highlight other experiments by users.

Further information on the NLUF is available by writing to:
> Thomas C. Bristow, Manager
> National Laser Users Facility
> Laboratory for Laser Energetics
> University of Rochester
> 250 East River Road
> Rochester, New York 14623

REFERENCES
1. H. Figueroa, C. Joshi, C. E. Clayton, H. Azechi, N. A. Ebrahim, and K. Estabrook, *UCLA Report* PPG-674 (1982).

PUBLICATIONS AND CONFERENCE PRESENTATIONS

Publications

S. D. Jacobs, "Liquid Crystals as Large Aperture Wave Plates and Circular Polarizers," *SPIE Vol. 307 Polarizers and Applications*, 98-105 (1982).

G. Mourou, W. Knox, and S. Williamson, "Advances in Picosecond Optoelectronics," *SPIE Vol. 322 Picosecond Lasers and Applications*, 107-114 (1982).

J. A. Valdmanis, G. Mourou, and C. W. Gabel, "Picosecond Electro-Optic Sampling System," *Appl. Phys. Lett.* **41**, 211-212 (1982).

G. M. Weyl, D. I. Rosen, J. Wilson, and W. Seka, "Laser-Induced Breakdown of Argon at $0.35\,\mu m$," *Phys. Rev. A* **26**, 1164-1167 (1982).

S. Kacenjar, S. Skupsky, A. Entenberg, L. Goldman, and M. Richardson, "Direct Measurement of the Fuel Density-Radius Product in Laser-Fusion Experiments," *Phys. Rev. Lett.* **49**, 463-467 (1982).

C. P. Verdon, R. L. McCrory, R. L. Morse, G. R. Baker, D. I. Meiron, and S. A. Orszag, "Nonlinear Effects of Multifrequency Hydrodynamic Instabilities on Ablatively Accelerated Thin Shells," *Phys. Fluids* **25**, 1653-1674 (1982).

H. Kim, T. Powers, and J. Mason, "Real-Time Parylene Coating-Thickness Measurement Using Optical Reflectometry," *J. Vac. Sci. Technol.* **21**, 900-901 (1982).

G. Mourou and S. Williamson, "Picosecond Electron Diffraction," *Appl. Phys. Lett.* **41**, 44-45 (1982).

Forthcoming Publications

B. Yaakobi, D. Villeneuve, M. Richardson, J. Soures, R. Hutchison, and S. Letzring, "X-Ray Spectroscopy Measurements of Laser-Compressed, Argon-Filled Shells," accepted for publication by *Optics Communications*.

R. Short, R. Bingham, and E. Williams, "Filamentation of Laser Light in Flowing Plasmas," accepted for publication by *Physics of Fluids*.

S. Jacobs, Y. Asahara, and T. Izumitani, "Optical Glass Wave Plates," accepted for publication by *Applied Optics*.

R. Marjoribanks, M. Richardson, J. Delettrez, S. Letzring, W. Seka, and D. Villeneuve, "Time-Resolved X-Ray Spectrometry of UV-Laser-Produced Plasmas," accepted for publication by *Optics Communications*.

K. Lee, "Comments on 'Transverse Electromagnetic Waves with $\vec{E} \parallel \vec{B}$,'" accepted for publication by *Physical Review Letters*.

R. Frankel and J. Forsyth, "Application of Nanosecond X-Ray Diffraction Techniques to Bacteriorhodopsin," accepted for publication by *Methods in Enzymology*.

S. Sarraf, E. Williams, and L. Goldman, "Ion-Ion Two-Stream Instability in Multispecies Laser-Produced Plasma," accepted for publication by *Journal of Physics A: General Physics*.

J. Reynolds, "Information Management Data Base in Fusion Targets," accepted for publication by *Journal of Vacuum Science and Technology*.

G. Albrecht, L. Lund, and D. Smith, "Building a Simple, Reliable, and Low-Cost Mode-Locker System," accepted for publication by *Applied Optics*.

T. Sizer II, "Synchronous Amplification of Subpicosecond Pulses," accepted for publication by *IEEE Journal of Quantum Electronics*.

Conference Presentations

W. Knox, G. Mourou, and S. Letzring, "Jitter-Free Signal-Averaging Streak Camera," presented at the Fifteenth International Congress on High-Speed Photography, San Diego, August 1982.

S. A. Letzring, R. S. Marjoribanks, and M. C. Richardson, "Time-Resolved X-Ray Spectrometry for Laser Fusion Studies," presented at the Fifteenth International Congress on High-Speed Photography, San Diego, August 1982.

R. S. Marjoribanks, M. C. Richardson, S. A. Letzring, and D. M. Villeneuve, "Time-Resolved X-Ray Spectroscopy of Symmetrically Imploded Targets," presented at the Fifteenth International Congress on High-Speed Photography, San Diego, August 1982.

G. Mourou, S. Letzring, and S. Williamson, "Picosecond Electron Diffraction," presented at the Fifteenth International Congress on High-

Speed Photography, San Diego, August 1982.

S. Kacenjar, S. Skupsky, A. Entenberg, L. Goldman, M. Richardson, and G. Korn, "Technique for Direct Measurement of Fuel Density-Radius Product in Laser Fusion," presented at the Fourth Topical Conference on High-Temperature Plasma Diagnostics, Boston, August 1982.

W. Knox and G. Mourou, "Jitter-Free Signal-Averaging Streak Camera and Applications in Picosecond Fluorescence Spectroscopy," presented at the American Chemical Society Meeting, Kansas City, Missouri, September 1982.

M. C. Richardson, T. Boehly, R. S. Craxton, J. Delettrez, G. D. Enright, A. Entenberg, R. Epstein, W. Friedman, J. Hoose, R. Hutchison, S. Kacenjar, K. Lee, S. Letzring, R. S. Marjoribanks, R. L. McCrory, J. Rizzo, W. Seka, R. Short, S. Skupsky, J. M. Soures, C. Verdon, D. M. Villeneuve, E. A. Williams, and B. Yaakobi, "Direct-Drive Laser Fusion Experiments with the OMEGA Laser System," presented at the International Atomic Energy Agency Ninth International Conference on Plasma Physics and Controlled Nuclear Fusion Research, Baltimore, September 1982.

W. Seka, L. M. Goldman, M. C. Richardson, J. M. Soures, D. M. Villeneuve, B. Yaakobi, R. S. Craxton, J. Delettrez, R. L. McCrory, R. Short, E. A. Williams, T. Boehly, R. L. Keck, K. Tanaka, and R. Boni, "Characteristics of UV-Laser-Matter Interactions," presented at the International Atomic Energy Agency Ninth International Conference on Plasma Physics and Controlled Nuclear Fusion Research, Baltimore, September 1982.